Available online at www.sciencedirect.com

ScienceDirect

Solid Earth Sciences 4 (2019) 43–65

www.elsevier.com/locate/SESCI

Trace element partitioning between $MgAl_2O_4$-spinel and carbonatitic silicate melt from 3 to 6 GPa, with emphasis on the role of cation order-disorder

Liping Liu [a,b], Yunlu Ma [a,b], Wei Yan [a,b], Xi Liu [a,b,*]

[a] School of Earth and Space Sciences, Peking University, Beijing, 100871, China
[b] Key Laboratory of Orogenic Belts and Crustal Evolution, Ministry of Education of China, Beijing, 100871, China

Received 17 May 2019; revised 24 May 2019; accepted 24 May 2019
Available online 13 June 2019

Abstract

To better understand the partitioning of trace elements between spinels and silicate melts at high *P*, a series of experiments have been conducted in the system $CaO–MgO–Al_2O_3–SiO_2–K_2O–CO_2$ at the *P-T* conditions of 3–6 GPa and 1500–1650 °C. These experiments successfully produced large $MgAl_2O_4$-spinel crystals coexisting with large carbonatitic silicate melt pools (plus large crystals of olivine and garnet in some cases). The experimental products were analyzed by using an electron microprobe in the wavelength-dispersive mode and an Agilent 7500 Ce laser ablation inductively-coupled plasma mass spectrometry, which led to high-*P* partition coefficients for 34 elements. The results suggest that pressure may have nominal significant impacts on the partition coefficients of some trace elements such as Nb, Ta, Ti, and nearly all rare earth elements (REEs), with the partition coefficients varying in several orders of magnitudes, but may play negligible roles in the partitioning of U, Mn, Fe, Sr, Ba, Na, K, Rb, and etc. Further analyses have revealed that much of the nominal *P* effects can be assigned to the Mg–Al cation order-disorder reaction. Cation exchange reactions are common in many geologically important minerals such as olivine, garnet, pyroxene, and plagioclase, and their effects on trace element partitioning should be extensively investigated in the near future before better understanding of the trace element partitioning systematics can be achieved. As one example, our experimental results have clearly demonstrated that due to much larger degrees of the Mg–Al cation order-disorder triggered by high *P*, spinel can strongly fractionate the REEs (with some heavy REEs compatible in the spinels and thus depleted in the relevant magmas), a phenomenon conventionally attributed to the presence of garnet. Some other important conclusions from our experiments include that Cr (or Ni) in the spinel structure at Cr-poor (or Ni-poor) conditions may be not as compatible as conventionally thought for Cr-rich (or Ni-rich) conditions, and Fe isotopes may be fractionated by spinels at high *P*.

Keywords: Cation order-disorder; High pressure experiment; Partition coefficient; Silicate magma; Spinel; Trace element

1. Introduction

Spinel (Sp) usually appears as an accessory mineral in common geological bodies (Dick and Bullen, 1984; Barnes and Roeder, 2001), but can volumetrically dominate some rocks, as demonstrated by some lunar meteorites (Gross and Treiman, 2011; Pieters et al., 2011). Comparing to common igneous minerals like olivine (Ol), Sp is relatively refractory and resistant to later alteration (Barnes and Roeder, 2001). Due to their universal appearance and excellent stability, Sp and its coexisting phases have been developed as geothermometer (Fabriès, 1979; Li et al., 1995), geobarometer (O'Neill, 1981; Zhang et al., 2016) and oxybarometer (O'Neill and Wall, 1987; Ballhaus et al., 1991). Furthermore, chromian Sp has been widely used as petrogenetic indicators in classifying mantle-derived peridotites (Dick and Bullen, 1984), exploring the melt compositional characteristics of the upper

* Corresponding author. School of Earth and Space Sciences, Peking University, Beijing, 100871, China. Fax: 86-10-6275-2996.
E-mail address: xi.liu@pku.edu.cn (X. Liu).
Peer review under responsibility of Guangzhou Institute of Geochemistry.

https://doi.org/10.1016/j.sesci.2019.05.002

mantle (Dick and Bullen, 1984; Arai, 1992; Liu and O'Neill, 2004a), probing the crystallization processes of basaltic magmas (Barnes and Roeder, 2001), reconstructing ancient tectonic settings (Cookenboo et al., 1997), and constraining the metamorphic evolutions of some ore deposits (Graham, 1978; Paraskevopoulos and Economou, 1981).

Although Sp is only an accessory mineral in most geological settings, with a content usually less than 1%, previous studies have indicated that many trace elements have large partition coefficients in Sp (e.g., Nielsen et al., 1994; Nielsen and Beard, 2000; Righter et al., 2006; Wijbrans et al., 2015). As some examples, the partition coefficient of Ni in magnetite is as high as 70, and that of Co is around 15 (Nielsen et al., 1994). These large partition coefficients mean that Sp might have significant impacts on the trace element budgets of the magmas. However, comparing to other common minerals like olivine and pyroxenes, studies of trace element partitioning behavior between the Sp and silicate melt are very rare, and mainly focus on the platinum group elements (Capobianco and Drake, 1990; Capobianco et al., 1994; Righter et al., 2004; Brenan et al., 2012), high field-strength elements and other transition metal elements (Horn et al., 1994; Nielsen et al., 1994; Nielsen and Beard, 2000; Davis et al., 2013). In particular, nearly all experiments have been conducted at 1 atm only (e.g., Nagasawa et al., 1980; Nielsen et al., 1992; Lundstrom et al., 2006; Wijbrans et al., 2015; Loroch et al., 2018), so that available experimental results could not tell us what happens under the mantle pressure conditions.

Sp has the space group $Fd\bar{3}m$, with two different cation sites (tetrahedral T-sites and octahedral M-sites) to accommodate the cations. The general formula of Sp is $^{[4]}(A_{1-x}B_x)^{[6]}(A_xB_{2-x})O_4$, where x is the inversion parameter ($x = 0$, normal Sp; $x = 1$, inverse Sp; $x = 0.667$, completely disordered Sp). As P, T and composition change, the Sp structure may change its order-disorder states, which in turn change the sizes of the T-sites and M-sites. For example, the $MgAl_2O_4$-Sp is generally a normal Sp under ambient conditions, but becomes partially or even fully disordered as T and P increase (e.g., Cynn et al., 1992, 1993; De Wijs et al., 2002; Méducin et al., 2004; Van Minh and Yang, 2004; Lazzeri and Thibaudeau, 2006; Slotznick and Shim, 2008; Liu et al., 2018). The bond length of its tetrahedron ($d_{T\text{-}O}$) is much longer than that of the octahedron ($d_{M\text{-}O}$) in the normal $MgAl_2O_4$-Sp, but is much shorter in the inverse $MgAl_2O_4$-Sp. The lattice strain model suggests that the partition coefficients of trace elements are related not only to the ionic radii and valence states of the substituting trace elements, but also to the sizes of the crystallographic sites of the host mineral (Brice, 1975; Blundy and Wood, 1994; Wood and Blundy, 1997). Therefore, the cation disordering process of the Sp caused by P and T variations potentially has significant impact on the partition behavior of trace elements.

In this study, we used some high-P experimental techniques to generate some large $MgAl_2O_4$-Sp crystals coexisting with large amounts of carbonatitic silicate melts in the system $CaO–MgO–Al_2O_3–SiO_2–K_2O–CO_2$ (CMAS-K_2O–CO_2) and analyzed the abundances of the trace elements. The experimental T range was from 1500 to 1650 °C, and the experimental P range was from 3 to 6 GPa. The aim of our work was two-fold, to constrain the partitioning behavior of some trace elements between the $MgAl_2O_4$-Sp and the silicate melt at high P-T conditions in specific, and to demonstrate the importance of cation disordering on the trace element partitioning in general.

2. Experimental and analytical methods

2.1. Starting materials

The starting materials, a broadly crystalline material and a fully glassy material, were made from mixtures of high-purity oxides (SiO_2, Al_2O_3 and MgO) and carbonates ($CaCO_3$ and K_2CO_3). The composition of the crystalline material was calculated by combining pure forsterite (Fo), orthopyroxene (Opx), clinopyroxene (Cpx) and garnet (Grt) in a weight proportion of 15:50:30:5, with the compositions of the Opx, Cpx and Grt from the experiment 34.6.3 in Gudfinnsson and Presnall (1996; 3.4 GPa and 1615 °C): 46.01% SiO_2, 11.02% Al_2O_3, 28.85% MgO, 7.91% CaO, and 6.22% CO_2. The weighted mixture was placed at 450 °C in a high-T furnace for 24 h to completely dry it, and then fully ground under acetone in an agate mortar. After that, it was kept at 110 °C in an oven for at least 24 h before it was loaded into a platinum capsule. The diameter of the capsule was ~5 mm and the length was ~3 mm. To synthesize the crystalline material, we performed a high-P experiment (LMD556) with the cubic press installed at the High-Pressure Laboratory of Peking University (Liu et al., 2012). The high-P assembly BJC-11 was adopted (He et al., 2014). The synthesizing P-T conditions were 4 GPa and 1600 °C, and the heating duration was 48 h. A small fraction of this experimental product was properly processed, and examined with a QUANTA-650FEG scanning electron microscopy (SEM) and a JXA-8100 electron microprobe (more later). We found the solid phases Ol, Grt, Sp and Cpx coexisting with a trace amount of CO_2-rich silicate melt. The compositions of these phases are listed in Table 1, and the proportions of these phases have been calculated as 27.3% Ol, 32.8% Grt, 1.9% Sp, 36.5% Cpx and 1.5% melt, using the MINSQ program (Herrmann and Berry,

Table 1
Major element compositions (wt%) of synthetic phases observed in the crystalline material.

Phase	CaO	MgO	Al_2O_3	SiO_2
Ol(8)[a]	0.30(5)[b]	58.17(32)	0.30(6)	41.64(34)
Grt(15)	8.94(279)	23.40(226)	23.94(33)	43.89(71)
Sp(12)	0.02(1)	29.47(21)	70.16(64)	0.94(26)
Cpx(13)	22.93(86)	18.68(159)	5.39(234)	52.46(175)
Melt(5)[c]	24.9(414)	18.30(352)	10.54(572)	10.51(191)

[a] Number after the phase is the number of the EMP analysis.
[b] Number in the parentheses is one standard deviation in the rightmost digit.
[c] The content of CO_2 in the melt is ~35.75%, as estimated by the EMPA-deficit method. Ol, olivine; Cpx, clinopyroxene; Grt, garnet; Sp, spinel.

2002). The most of this experimental product was finely ground, and used in our later high-*P* experiments.

The composition of the melt from the experiment 34.6.3 in Gudfinnsson and Presnall (1996) was first normalized to 97 wt %, and then added with 3% K_2O (as K_2CO_3). After fully ground in an agate mortar under acetone, this mixture was stored in an oven at 110 °C for more than 24 h. It was eventually put into a platinum crucible, and melted for 30 min at 1600 °C in a high-*T* furnace, and quenched. The resulted glassy material was crashed, ground and homogenized under acetone, and stored in an oven at 110 °C for later high-*P* experiments.

It should be noted that no trace elements were intentionally added to any of the two starting materials. According to Horn et al. (1994), the concentrations of certain trace elements in the spinel should be less than 1 wt% in order to meet the Henry's law. Indeed Righter et al. (2006) revealed large differences in the partition coefficients of some trace elements obtained from doped and undoped experiments. The abundances of the trace elements in our experiments must have been very low, so that their partitioning behaviors between the solid phases and the melts observed in this study should obey the Henry's law in general.

2.2. High-P equilibrium experiments

All our high-*P* equilibrium experiments were made on the cubic press using the assembly BJC-11. For every experiment, ~10–12 mg starting materials were loaded into a Pt capsule of 2 mm diameter. In order to minimize quench effect on the melt, the sandwich experimental method was adopted, with the crystalline material placed at the top and bottom of the capsule, and the glassy material loaded in the middle (Liu and O'Neill, 2004b). To avoid the contamination of air water, the loaded Pt capsule was stored at 110 °C for at least 24 h before welded, and the used experimental parts such as the hBN sleeve were always stored in an oven at 60 °C. The experimental *T* was controlled to ±1 °C by using a W/Re thermocouple and the experimental *P* was controlled to ±0.05 GPa. The experimental conditions are listed in Table 2.

Our primary goal of this study was to constrain the partitioning behavior of some trace elements between the Sp and the silicate melts, so that a good equilibrium between the solid phases and the melts was of great importance. Existing experimental studies in the CMAS system (e.g., Presnall et al., 1978; Sen and Presnall, 1984; Liu and Presnall, 1990) suggested that 8 h was long enough to achieve good equilibrium for the phase assemblages similar to those observed here, as long as the melt fraction was high. The reaction time of our experiments was accordingly set as ≥ 12 h. As revealed later, the compositions of the solid phases in our experimental products are very homogeneous, indicating good chemical equilibrium practically established in our experiments.

Table 2
Experimental conditions and observed phases.

Exp. #	Ratio[a]	*P*(GPa)	*T*(°C)	*t*(h)	Phases[b]
LMD565	1:0.8:1	3	1500	36	Sp+Melt
LMD564	1:1.25:1	4	1500	36	Sp+Melt
LMD563	1:1:1	4	1550	24	Sp+Melt
LMD558	1:1.25:1	4	1550	36	Sp+Ol+Melt
LMD578	1:1.25:1	5	1630	12	Sp+Grt+Melt
LMD568	1:1.25:1	6	1650	12	Sp+Grt+Melt

[a] All experiments were conducted with an initial "sandwich" sample arrangement, with the crystalline material placed at the top and bottom of the capsule, and with the glassy material placed in the middle. The listed ratios are in wt%.

[b] Sp, spinel; Ol, olivine; Grt, garnet.

2.3. Analytical procedures

The experimental products were mounted with epoxy and polished with a series of diamond pastes. Coexisting phases in all experimental products were identified by using the QUANTA-650FEG SEM. Their major element contents were obtained using the JXA-8100 electron microprobe in the wavelength-dispersive mode, with an accelerating voltage of 15 keV and a beam current of 10 nA. The solid phases were analyzed with a 1-μm focused beam. The well-quenched melt was also analyzed with the 1-μm focused beam, but the poorly-quenched melt with numerous tiny non-equilibrium crystals was analyzed with a 5-μm defocused beam. To avoid K evaporating, K was analyzed first. The PRZ correction procedure was applied to all the electron microprobe analyses (EMPA). The major element compositions of the observed phases in our experiments are listed in Tables 3 and 4.

The trace element compositions were analyzed using an Agilent 7500 Ce laser ablation inductively-coupled plasma mass spectrometry (LA-ICP-MS) at the School of Earth and Space Sciences, Peking University. The LA-ICP-MS system was coupled to a COMPexPro 102 laser-ablation system with a 193 nm ArF-excimer laser. Helium was served as carrier gas to enhance the transport efficiency of the ablated material. A repetition rate of 5 Hz and a laser energy of 100 mJ were used in this study. The beam size of the laser for the Sp analyses was mostly 60-μm in diameter, but in some cases adjusted to 14-μm in diameter in order to avoid any contamination of surrounding melts. Other coexisting crystalline phases like the Ol and Grt were also analyzed with the 14-μm spot size. The melts were analyzed with a spot size of either 60 or 120-μm, as large melt patches were produced in every experiment reported here. The background acquisition time and the data acquisition interval were 20 s (including 5 s pre-ablation) and 60 s, respectively (Li et al., 2013).

All measurements were performed using the NIST 610 glass as external standard and the NIST 612 and 614 glasses as monitoring standards (Jochum et al., 2011). The Mg^{24} contents obtained from the EMPA were used as internal standards for the Sp, Ol and Grt measurements. Due to quench modification, the Mg^{24} contents of the melts in some experiments were of relatively high uncertainty (Table 4), and the Al^{27} contents were then used as the internal standards in these cases. Detection limits were not constant as they could vary with the beam diameter and equipment conditions (Lazartigues et al., 2014);

Table 3
Major element compositions (wt%) of minerals.

Exp. #	LMD565	LMD564	LMD563	LMD558		LMD578		LMD568	
P/T[a]	3/1500	4/1500	4/1550	4/1550		5/1630		6/1650	
Phase	Sp(8)[b]	Sp(8)	Sp(7)	Sp(5)	Ol(5)	Sp(13)	Grt(10)	Sp(13)	Grt(9)
CaO	0.01(1)[c]	0.02(2)	0.01(1)	0.00(0)	0.17(1)	0.01(1)	4.07(92)	0.02(1)	3.98(73)
MgO	28.66(25)	29.26(15)	28.44(22)	29.01(30)	58.20(84)	28.94(18)	27.52(70)	29.13(26)	27.75(68)
Al_2O_3	70.23(53)	70.29(18)	70.92(33)	69.98(60)	0.39(2)	70.22(25)	24.77(25)	69.27(59)	24.46(24)
SiO_2	0.39(5)	0.65(7)	0.30(7)	0.76(3)	41.49(72)	0.76(7)	44.44(18)	1.03(7)	44.12(29)
Total	99.29(72)	100.22(30)	99.68(35)	99.75(86)	100.26(54)	99.92(36)	100.79(10)	99.45(78)	100.31(36)

[a] Pressure and temperature in GPa and °C, respectively.
[b] Number after the phase is the number of the EMPA.
[c] Number in the parentheses is one standard deviation in the rightmost digit.

Table 4
Major element compositions (wt%) of melts.

Exp. #	n[a]	K_2O	CaO	MgO	Al_2O_3	SiO_2	CO_2[b]	*P/T*[c]
LMD565	8	0.70(3)[d]	7.31(18)	29.21(33)	17.35(33)	27.77(20)	17.66	3/1500
LMD564	9	0.82(42)	7.61(138)	40.03(378)	11.14(45)	21.58(45)	18.82	4/1500
LMD563	8	1.36(13)	9.85(16)	22.40(10)	22.80(20)	22.37(16)	21.22	4/1550
LMD558	5	1.78(10)	11.23(8)	38.17(35)	8.71(15)	18.75(18)	21.36	4/1550
LMD578	11	1.23(6)	8.65(24)	29.10(26)	16.79(40)	28.42(17)	15.81	5/1630
LMD568	7	0.85(45)	9.00(143)	31.02(194)	15.59(58)	26.49(40)	17.05	6/1650

[a] Number of the EMPA performed.
[b] Content of CO_2 is calculated by the EMPA-deficit method.
[c] Pressure and temperature in GPa and °C, respectively.
[d] Number in the parentheses is one standard deviation in the rightmost digit.

for example, their values for most rare earth elements (REEs) ranged from 0.001 to 0.20 ppm, as observed in this study. Trace element values were processed with the Glitter software (Jackson, 2001), and the results are listed in Tables 5 and 6.

3. Results and discussions

3.1. Phase assemblages

All experimental products contain large Sp crystals and large melt pools, with some having additional phase such as Ol or Grt (Fig. 1 and Table 2). The Sp grains are typically idiomorphic, their sizes range from ~50 to 600 μm (Fig. 1), and their compositions are very homogeneous (Table 3). Grt has been observed in two experiments (LMD578 and LMD568), and it appears idiomorphic (5–30 μm) but shows slight compositional heterogeneity. A large Ol crystal has been observed in LMD558, surrounding one large Sp grain. Its composition is close to pure Fo (Table 3).

The melt phases in different experiments show different quench features. In LMD565 (Fig. 1a), LMD563 (Fig. 1c), LMD558 (Fig. 1g) and LMD578 (Fig. 1h), large pockets of well-quenched melts have been found, and their major element compositions have been well characterized by the EMPA (Table 4). In contrast, the melts in LMD564 (Fig. 1b) and LMD568 (Fig. 1f) contain numerous tiny quench crystals, so that their EMPA results show some compositional scattering, especially those regarding to the MgO and CaO components (Table 4). The quench phase/phases in our experiments could be MgO- and CaO-rich.

In addition, numerous small circular holes have been observed in our experimental products (Fig. 1g). Their presence might suggest that our experiments were saturated with a CO_2-rich volatile phase, implying a high oxygen fugacity (f_{O2}) in these experiments.

3.2. Phase compositions

The Sp observed in our experimental products is almost pure $MgAl_2O_4$, with small amounts of SiO_2 though (0.3–1.03 wt%; Table 3). A charge balance reaction, with one Si^{4+} and one Mg^{2+} substituting for two Al^{3+}, has been observed and reported in Liu et al. (2018). As the experimental *P-T* conditions change from ~3 to 4 GPa and 1500 °C to ~5–6 GPa and 1630–1650 °C, the Si cations radically change from being fully ordered on the T-sites to randomly distributing between the T-sites and the M-sites (Liu et al., 2018).

The Ol observed in LMD558 is nearly pure Fo, with small amounts of Al_2O_3 (~0.39%) and CaO (~0.17%; Table 3). The low CaO content of the Ol may reflect the low CaO content in the coexisting melt (Table 4).

The Grt observed in LMD578 and LMD568 are generally solid solutions between the endmember pyrope ($Mg_3Al_2Si_3O_{12}$) and the endmember grossular ($Ca_3Al_2Si_3O_{12}$), with the former predominating (Table 3).

The melt compositions are shown in Table 4. The SiO_2 content ranges from 18.75 to 28.42%, the Al_2O_3 from 8.71 to 22.80%, the MgO from 22.40 to 40.03%, the CaO from 7.31 to 11.23%, and the K_2O from 0.70 to 1.78%. The CO_2 content has been determined with the EMPA-deficit method, and

Table 5
Results of LA-ICP-MS analyses of spinel and melt (ppm), and the partition coefficients.

Exp. #	LMD565			LMD564		
P/T	3 GPa/1500 °C			4 GPa/1500 °C		
Phase	Sp(7)[a]	Melt(6)	D_{sp}(6)	Sp(6)	Melt(6)	D_{sp}(6)
Na^{23}	9.9	237.6(11)[b]	0.042	b.d.l.[c]	395(16)	
Si^{29}	4650(460)	135659(1401)	0.034(3)	6392(1036)	105360(5074)	0.061(10)
P^{31}	27.3(59)	19.2(17)	1.42(31)	22.2(2)	23.6(23)	0.941(7)
K^{39}	b.d.l.	9683(77)		52.6(277)	13161(615)	0.004(2)
Ca^{43}	166(22)	53705(395)	0.003(0)	343.9	65120(2787)	0.005
Ti^{49}	1.59	1.319(327)	1.205	0.99	2.983(716)	0.332
Cr^{53}	12.3(22)	0.86	14.3(26)	26.21	1.73	15.15
Mn^{55}	1.81	0.577(262)	3.14	b.d.l.	1.176(439)	
Fe^{56}	57.3(234)	8.0(31)	7.1(29)	34.7(159)	3.4(35)	10.2(47)
Fe^{57}	b.d.l.	10.1(6)		20.6(34)	10.6(9)	1.94(32)
Ni^{60}	0.34	0.234(13)	1.456	0.223	0.296(18)	0.755
Rb^{85}	0.056	0.502(9)	0.111	b.d.l.	0.642(42)	
Sr^{88}	0.042(9)	28.843(310)	0.0015(3)	0.14(10)	37.1(18)	0.004(3)
Y^{89}	0.028	3.183(60)	0.009	0.0417	7.33(34)	0.006
Nb^{93}	0.0166	0.00087	19.08	0.0213	b.d.l.	
Sn^{118}	0.538(55)	2.9(11)	0.185(19)	0.61(17)	1.37(41)	0.44(13)
Ba^{137}	0.185(23)	10.658(79)	0.017(2)	b.d.l.	12.71(58)	
La^{139}	0.0207	4.533(59)	0.005	0.035	5.93(28)	0.006
Ce^{140}	0.0222	1.992(23)	0.011	0.036(21)	6.27(28)	0.006(3)
Pr^{141}	0.0195	0.380(12)	0.051	0.0277	0.885(41)	0.031
Nd^{146}	b.d.l.	1.812(56)		0.150(67)	4.13(19)	0.036(16)
Sm^{147}	b.d.l.	0.395(16)		0.132	0.899(60)	0.147
Eu^{153}	0.051(13)	0.094(5)	0.54(14)	b.d.l.	0.210(11)	
Gd^{157}	b.d.l.	0.471(17)		0.214	0.910(54)	0.235
Tb^{159}	0.0138	0.076(2)	0.182	b.d.l.	0.153(10)	
Dy^{163}	b.d.l.	0.471(19)		b.d.l.	1.065(55)	
Ho^{165}	0.0148	0.089(3)	0.166	0.0201	0.238(12)	0.084
Er^{166}	0.074	0.198(12)	0.374	b.d.l	0.650(36)	
Tm^{169}	b.d.l.	0.021(2)		b.d.l.	0.096(6)	
Yb^{172}	0.095	0.134(10)	0.711	0.16	0.599(37)	0.267
Lu^{175}	b.d.l.	0.020(1)		b.d.l.	0.085(3)	
Ta^{181}	b.d.l.	b.d.l.		0.0304	0.002(0)	20.000
Pb^{208}	b.d.l.	b.d.l.		b.d.l.	0.012(7)	
Th^{232}	b.d.l.	0.194(9)		b.d.l.	0.698(26)	
U^{238}	0.067	0.104(6)	0.643	b.d.l.	0.935(52)	

Exp. #	LMD563			LMD558		
P/T	4 GPa/1550 °C			4 GPa/1550 °C		
Phase	Sp(6)	Melt(7)	D_{sp}(6)	Sp(10)	Melt(8)	D_{sp}(8)
Na^{23}	5.9(20)	366.2(32)	0.016(6)	6.3(11)	646.2(26)	0.010(2)
Si^{29}	2771(463)	106074(690)	0.026(4)	5069(200)	91908(295)	0.055(2)
P^{31}	46(13)	25.4(53)	1.82(51)	40.3(93)	32.8(44)	1.23(28)
K^{39}	5.4(28)	16113(177)	0.0003(2)	5.5(19)	18252(138)	0.0003(1)
Ca^{43}	175(90)	73053(1148)	0.002(1)	149(39)	84348(522)	0.002(0)
Ti^{49}	0.70(11)	4.91(52)	0.143(23)	0.857(55)	1.79(25)	0.479(31)
Cr^{53}	3.9(8)	1.3(2)	2.95(63)	2.7(3)	1.2(2)	2.24(27)
Mn^{55}	1.38(55)	1.94(44)	0.71(28)	b.d.l.	0.585(92)	
Fe^{56}	45(25)	6.76	6.7(36)	30(14)	10.3(55)	2.9(14)
Fe^{57}	11.28	14.4(18)	0.781	10.98	18.5(16)	0.593
Ni^{60}	0.337(6)	0.27(23)	1.238(21)	0.337(6)	0.216(56)	1.559(26)
Rb^{85}	0.086	0.826(12)	0.104	0.042	0.898(23)	0.047
Sr^{88}	0.024(7)	45.79(76)	0.0005(2)	0.021(3)	57.31(54)	0.0004(1)
Y^{89}	0.069(64)	178.5(41)	0.0004(4)	b.d.l.	9.49(14)	
Nb^{93}	0.0227	0.0058	3.914	b.d.l.	0.010(1)	
Sn^{118}	–	–		–	–	
Ba^{137}	b.d.l.	14.86(49)		0.202	20.37(33)	0.010
La^{139}	0.0264	48.9(12)	0.001	b.d.l.	24.83(23)	
Ce^{140}	0.0177	4.04(11)	0.004	0.0218	7.215(83)	0.003
Pr^{141}	b.d.l.	0.62(2)		0.015(3)	1.047(25)	0.014(3)

(*continued on next page*)

Table 5 (*continued*)

Exp. #	LMD563			LMD558		
P/T	4 GPa/1550 °C			4 GPa/1550 °C		
Phase	Sp(6)	Melt(7)	D_{sp}(6)	Sp(10)	Melt(8)	D_{sp}(8)
Nd^{146}	b.d.l.	2.719(95)		0.062	4.74(12)	0.013
Sm^{147}	0.142	0.513(37)	0.277	0.110(38)	0.993(64)	0.111(38)
Eu^{153}	b.d.l.	0.142(9)		b.d.l.	0.255(11)	
Gd^{157}	0.143	0.604(21)	0.237	0.113	0.982(42)	0.115
Tb^{159}	b.d.l.	0.100(7)		0.0245	0.163(7)	0.150
Dy^{163}	b.d.l.	0.572(32)		0.071(11)	1.026(35)	0.069(10)
Ho^{165}	0.0152	0.129(11)	0.118	0.0145	0.235(13)	0.062
Er^{166}	b.d.l	0.280(18)		b.d.l.	0.611(20)	
Tm^{169}	b.d.l.	0.037(5)		0.0202	0.083(4)	0.242
Yb^{172}	0.132	0.187(32)	0.707	b.d.l.	0.536(43)	
Lu^{175}	b.d.l.	0.029(4)		b.d.l.	0.071(7)	
Ta^{181}	b.d.l.	0.016(10)		0.0181	0.0104	1.740
Pb^{208}	b.d.l.	0.023(3)		0.095(17)	0.018(6)	5.36(99)
Th^{232}	b.d.l.	0.269(12)		b.d.l.	0.763(27)	
U^{238}	b.d.l.	0.337(26)		0.0245	0.317(25)	0.077
Exp. #	LMD578			LMD568		
P/T	5 GPa/1630 °C			6 GPa/1650 °C		
Phase	Sp(6)	Melt(5)	D_{sp}(5)	Sp(6)	Melt(7)	D_{sp}(6)
Na^{23}	b.d.l.	356.1(57)		9.3	376.7(34)	0.025
Si^{29}	6663(223)	137759(1146)	0.048(2)	6313(740)	116944(4101)	0.054(6)
P^{31}	39(13)	17.6(13)	2.22(74)	41(11)	18.7(21)	2.18(59)
K^{39}	24(19)	12929(360)	0.002(1)	9.4(19)	11430(1977)	0.001(0)
Ca^{43}	212(124)	60607(296)	0.004(2)	151(36)	57828(2596)	0.003(1)
Ti^{49}	2.20(76)	5.8(12)	0.38(13)	1.78(67)	13.6(23)	0.131(49)
Cr^{53}	21(12)	1.3(7)	16.3(93)	6.7(8)	1.6(2)	4.29(54)
Mn^{55}	2.41	0.97(25)	2.486	1.74	1.48(39)	1.179
Fe^{56}	34.32	3.7(18)	9.396	40.1(84)	3.6(12)	11.2(23)
Fe^{57}	b.d.l.	11.0(11)		28.95	13.0(5)	2.227
Ni^{60}	0.71(18)	0.38(27)	1.86(48)	1.9(19)	0.51(79)	3.8(38)
Rb^{85}	b.d.l.	0.641(14)		0.112(18)	0.63(10)	0.179(29)
Sr^{88}	0.066(43)	35.72(39)	0.002(1)	0.045(13)	36.4(49)	0.001(0)
Y^{89}	0.0157	3.482(66)	0.005	b.d.l.	3.02(24)	
Nb^{93}	0.0227	0.003(1)	8.007	0.038(1)	0.004(2)	8.59(16)
Sn^{118}	0.63(13)	1.80(69)	0.348(72)	–	–	
Ba^{137}	0.305(93)	13.11(11)	0.023(7)	0.290(76)	28.2(49)	0.010(3)
La^{139}	0.071(83)	28.66(28)	0.002(3)	0.041	8.9(13)	0.005
Ce^{140}	b.d.l.	2.432(15)		b.d.l.	2.74(38)	
Pr^{141}	0.031(14)	0.474(7)	0.065(29)	0.0299	0.511(71)	0.059
Nd^{146}	0.14(10)	2.291(32)	0.063(45)	b.d.l.	2.39(31)	
Sm^{147}	0.124(17)	0.479(9)	0.259(35)	b.d.l.	0.488(50)	
Eu^{153}	b.d.l.	0.116(9)		b.d.l.	0.120(16)	
Gd^{157}	b.d.l.	0.535(23)		b.d.l.	0.522(70)	
Tb^{159}	0.026(4)	0.082(5)	0.312(45)	b.d.l.	0.086(11)	
Dy^{163}	b.d.l.	0.504(17)		b.d.l.	0.502(55)	
Ho^{165}	b.d.l.	0.090(4)		b.d.l.	0.091(9)	
Er^{166}	b.d.l.	0.193(10)		b.d.l.	0.188(22)	
Tm^{169}	0.0108	0.025(0)	0.432	0.034(2)	0.021(2)	1.589(93)
Yb^{172}	0.127(23)	0.142(10)	0.89(16)	0.181	0.122(12)	1.483
Lu^{175}	0.0249	0.016(1)	1.557	b.d.l.	0.015(2)	
Ta^{181}	0.0264	0.004(1)	7.281	0.031	0.007(3)	4.242
Pb^{208}	b.d.l.	0.0109		0.136	0.031(13)	4.335
Th^{232}	0.0244	0.182(7)	0.134	b.d.l.	0.244(40)	
U^{238}	0.043(17)	0.220(6)	0.196(76)	0.06	0.151(26)	0.398

[a] Number of analysis spot.
[b] Number in parentheses is 1 SD; 237.6(11) read as 237.6 ± 1.1.
[c] b.d.l., below detection limit.

Table 6
Results of LA-ICP-MS analyses of olivine and garnet (ppm), and the partition coefficients.

Exp. #	LMD558		LMD578		LMD568	
P/T	4 GPa/1550 °C		5 GPa/1630 °C		6 GPa/1650 °C	
Phase	Ol(6)[a]	D_{ol}(6)	Grt(5)	D_{grt}(5)	Grt(6)	D_{grt}(6)
Na^{23}	3.1(5)[b]	0.005(1)	169(104)	0.48(29)	102.3(73)	0.272(19)
Si^{29}	218229(406)	2.37(0)	165184(36617)	1.20(27)	247261(6537)	2.114(56)
P^{31}	36(3)	1.097(93)	95.4	5.409	b.d.l.[c]	
K^{39}	36(42)	0.002(2)	5676(4544)	0.44(35)	735(965)	0.064(84)
Ca^{43}	1422(26)	0.017(0)	35910(14589)	0.59(24)	31044(3798)	0.537(66)
Ti^{49}	0.41(11)	0.231(59)	7.910	1.361	15.8(53)	1.17(39)
Cr^{53}	1.32(50)	1.08(41)	b.d.l.		52.210	33.499
Mn^{55}	0.43(11)	0.73(18)	10.8(30)	11.2(31)	22.400	15.184
Fe^{56}	15.3(73)	1.48(71)	173.0(84)	47.4(23)	140(39)	39(11)
Fe^{57}	b.d.l.		86(21)	7.8(19)	129(21)	10.0(16)
Ni^{60}	0.232(53)	1.07(25)	1.520	3.981	2.923(911)	5.8(18)
Rb^{85}	0.017	0.019	0.38(14)	0.58(22)	b.d.l.	
Sr^{88}	0.133(95)	0.002(2)	17(14)	0.47(39)	2.843(3310)	0.08(9)
Y^{89}	0.086(8)	0.009(1)	3.34(46)	0.96(13)	3.737(708)	1.24(23)
Nb^{93}	0.006(0)	0.593(28)	0.112	39.506	b.d.l.	
Sn^{118}	–		1.430	0.794	–	
Ba^{137}	b.d.l.		6.1(39)	0.46(30)	4.830(2234)	0.172(79)
La^{139}	0.041(47)	0.002(2)	13(11)	0.46(39)	0.952(871)	0.107(98)
Ce^{140}	0.016(12)	0.002(2)	1.42(77)	0.58(32)	0.546(375)	0.20(14)
Pr^{141}	0.008	0.008	0.32(20)	0.67(43)	0.199	0.389
Nd^{146}	b.d.l.		2.12(40)	0.92(18)	1.745(643)	0.73(27)
Sm^{147}	0.058(17)	0.058(17)	0.910	1.900	b.d.l.	
Eu^{153}	b.d.l.		0.189(6)	1.632(49)	b.d.l.	
Gd^{157}	b.d.l.		0.98(30)	1.82(57)	b.d.l.	
Tb^{159}	b.d.l.		0.132(19)	1.60(23)	0.276(81)	3.20(93)
Dy^{163}	0.027	0.026	0.55(14)	1.09(27)	1.290	2.568
Ho^{165}	0.007	0.028	0.114(18)	1.26(20)	0.300(86)	3.31(95)
Er^{166}	0.015	0.025	0.290	1.502	0.750	3.981
Tm^{169}	b.d.l.		b.d.l.		0.289	13.586
Yb^{172}	0.036(4)	0.067(8)	0.400	2.814	1.340	10.980
Lu^{175}	0.012(2)	0.167(24)	b.d.l.		0.251(58)	16.5(38)
Ta^{181}	b.d.l.		0.110	30.336	b.d.l.	
Pb^{208}	0.046(5)	2.59(31)	0.850	77.982	b.d.l.	
Th^{232}	b.d.l.		b.d.l.		b.d.l.	
U^{238}	b.d.l.		b.d.l.		b.d.l.	

[a] Number of analysis spot.
[b] Number in parentheses is 1 SD; 3.1(5) read as 3.1 ± 0.5.
[c] b.d.l., below detection limit.

ranges from 15.81% to 21.36%. According to Dalton and Presnall (1998), the thus-obtained CO_2 contents in our silicate melts are reasonable. In addition, small amounts of H_2O (presumably < 0.5 wt%) might appear in the melts, as a completely dry experimental condition could not be practically maintained, especially when small pyrophyllite parts were used in the high-*P* experiments (Canil and Scarfe, 1990; Gudfinnsson and Presnall, 1996; Dalton and Presnall, 1998; Liu et al., 2006). Summarily the melts produced by our high-*P* experiments were generally MgO-rich carbonatitic silicate melts.

3.3. Distribution of Si, Ca, Cr and Ni between spinels and silicate melts

The major element compositions of natural spinels in various geological bodies from different tectonic environments were commonly analyzed, the data were frequently compiled, and the implications were regularly explored (e.g., Roeder, 1994; Barnes, 1998; Barnes and Roeder, 2001; Kamenetsky et al., 2001). In contrast, the major element compositions of spinels from experiments were much less reported, mainly due to their small grain sizes and low proportions usually encountered in the experiments (Roeder and Reynolds, 1991; Liu and O'Neill, 2004b). Here, we briefly summarize the compositional data for some major elements (Si, Ca, Cr and Ni) in some synthetic spinels in equilibrium with silicate melts, and tentatively probe the distribution features. Strictly speaking, Ca cannot be treated as a major element because of its low abundance in the spinels. Nevertheless, it is abundant in most magmas.

To facilitate our discussion, we have chosen to use the Nernst's partition coefficient, a term most appropriate for the partitioning process of trace elements. The Nernst's partition

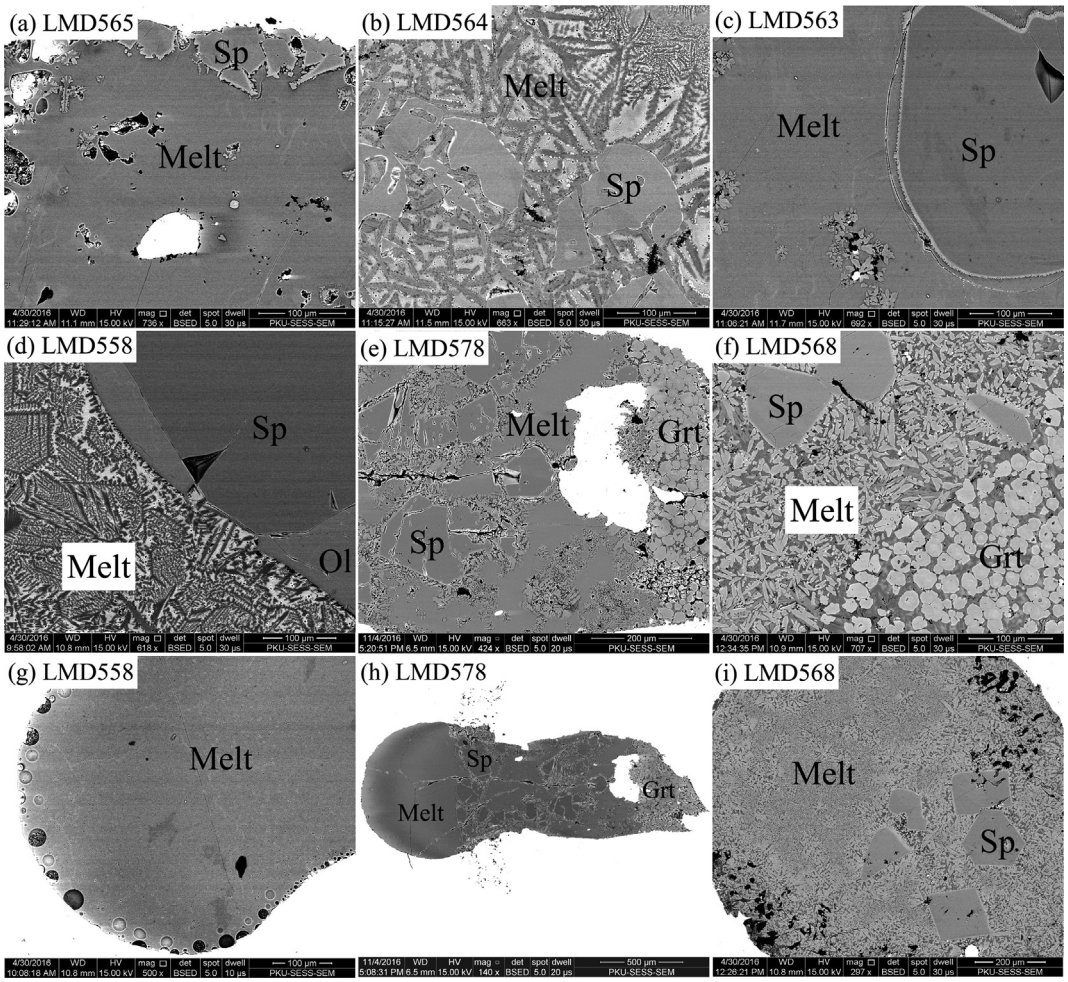

Fig. 1. Typical electron back-scatter images for the coexisting of large $MgAl_2O_4$-spinel crystals and melt pockets in LMD565 (a), LMD564 (b), LMD563 (c), LMD558 (d), LMD578 (e), and LMD568 (f); and additional electron back-scatter images for the melt region of LMD558 (g), for the entire charge of LMD578 (h), and for a large portion of LMD568 (i). See Table 2 for the experimental *P-T* conditions and other details. Presumably due to the combined effects of high experimental *T*, large proportion of melt, and strong corrosive nature of carbonatitic silicate melt, some Pt capsules showed signs of melting to some degree or alloying with the experimental charge. Furthermore, it is rather unclear whether all tiny crystals in LMD563 (c) and LMD568 (f) were formed during quenching or not, due to the slightly larger sizes attained by some of the crystals than what we usually find out for quench phases. To be conservative, the melt regions teemed with these relatively larger crystals were avoided in our EMP and LA-ICP-MS analyses.

coefficient describes the partition behavior of an element *i* between a mineral and a coexisting melt phase, and is defined as follows

$$D^i_{mineral} = C^i_{mineral} / C^i_{melt} \quad (1)$$

where $C^i_{mineral}$ and C^i_{melt} are the weight fractions of the element *i* in the mineral and the melt (in ppm), respectively (Nernst, 1891). When $D^i_{mineral} > 1$, the element *i* is a compatible element, and tends to concentrate in the solid phase; when $D^i_{mineral} < 1$, the element is an incompatible element, and enriches in the melt phase. During the process of partitioning an element *i* between a mineral and a melt phase, $D^i_{mineral}$ should be a constant if the partition process obeys the Henry's law (i.e., $D^i_{mineral}$ being independent to either $C^i_{mineral}$ or C^i_{melt}).

Si The D^{Si}_{Sp} constrained by our experiments ranges from 0.026(4) to 0.061(10) (Table 5; averagely 0.046(13)), slightly larger than the values obtained by Loroch et al (2018; Fig. 2a). Si is thus highly incompatible in the $MgAl_2O_4$-Sp structure. This can be understood in terms of the differences of the charge states and the cation radii: Si is 4+, compared to 2+ for Mg and 3+ for Al; the cation radii of Si^{4+} in four-fold coordination and six-fold coordination are respectively 0.26 and 0.4 Å, much smaller than those values for the Mg^{2+} (respectively 0.57 and 0.72 Å), and those values for the Al^{3+} (respectively 0.39 and 0.535 Å; Shannon, 1976). As larger Cr and Fe cations enter the $MgAl_2O_4$-Sp structure, the dimensions of the unit cell and the size of the cation sites are expected to expand, so that Si should become even more incompatible. This is well illustrated in Fig. 2a (compare the symbols in black to the symbols in color). In comparison, pressure may play a different role, reducing the size of the cation sites to some degrees and making Si more compatible (compare the squares to all other symbols). Further, the coupled substitution of $Si^{4+} + Mg^{2+} = 2Al^{3+}$, as observed by Liu et al. (2018), should also play an important role in the Si

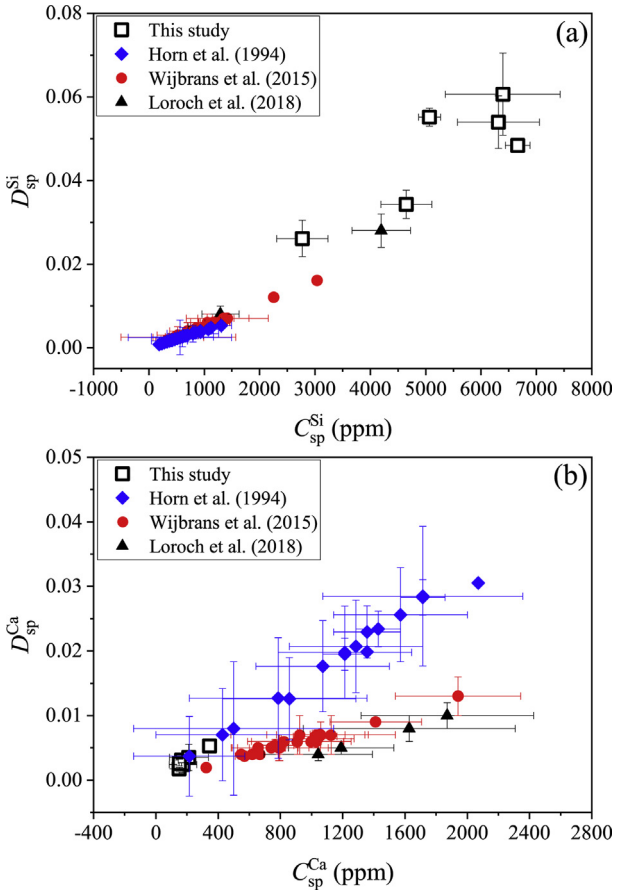

Fig. 2. D^{Si}_{Sp} vs C^{Si}_{Sp} (a) and D^{Ca}_{Sp} vs C^{Ca}_{Sp} (b). The spinels from this study (3–6 GPa and 1500–1650 °C) and Loroch et al. (2018; 1 atm and 1000–1350 °C) were generally $MgAl_2O_4$-Sp (i.e., without significant Cr or Fe). In contrast, the spinels from Horn et al. (1994) contained various amounts of Cr_2O_3 (0–56.17 wt%) and FeO_t (14.48–68.03 wt%; $FeO_t = FeO + Fe_2O_3$), as they were obtained with a natural alkali olivine basalt (1 atm, 1235–1340 °C and $\log f_{O2} = -8.28$ to -0.68). The spinels from Wijbrans et al. (2015) also contained various amounts of Cr_2O_3 (0–30.2 wt%) and FeO_t (0–62.4 wt%; 1 atm, 1220–1450 °C and $\log f_{O2} = -12$ to -0.7).

incorporation into the spinel structure. Overall, the D^{Si}_{Sp} is well related to the C^{Si}_{Sp}, $D^{Si}_{Sp} = 8.71(23) \times 10^{-6} \times C^{Si}_{Sp} - 0.0028(4)$ ($R^2 = 0.95$). Once the C^{Si}_{Sp} is known, the D^{Si}_{Sp} can be calculated, and the Si content in the silicate melts in equilibrium can eventually be constrained.

Ca The D^{Ca}_{Sp} constrained by our experiments is mostly <0.005 (Table 5), with small differences to the values obtained by Loroch et al (2018; Fig. 2b). Ca is thus strongly incompatible in the $MgAl_2O_4$-Sp structure, a characteristic almost independent to the melt compositions (e.g., CO_2-rich and CO_2-free silicate melts in this study and Loroch et al. (2018), respectively) and P (e.g., 3–6 GPa and 1 atm in this study and Loroch et al. (2018), respectively). This can be understood in terms of the significant differences of the cation radii: the effective cation radius of Ca^{2+} in six-fold coordination is 1.0 Å, much larger than those values for Mg^{2+} and Al^{3+} (respectively 0.72 and 0.535 Å; Shannon, 1976). As larger Cr and Fe cations enter the $MgAl_2O_4$-Sp structure, further, the dimensions of the unit cell and the size of the cation sites should expand, and more Ca may enter the spinel structure. Indeed, the 1-atm spinels from Loroch et al. (2018) were free of Cr and Fe and had the smallest D^{Ca}_{Sp}, the 1-atm spinels from Horn et al. (1994) had the highest Cr and Fe contents and attained the largest D^{Ca}_{Sp}, and the 1-atm spinels from Wijbrans et al. (2015) had intermediate Cr and Fe contents and attained intermediate D^{Ca}_{Sp} (Fig. 2b).

Cr The D^{Cr}_{Sp} constrained by our experiments ranges from 2.2(3) to 16(9) (Table 5; averagely 9.2(67)), remarkably smaller than the values obtained by other studies at Cr-rich conditions ($D^{Cr}_{Sp} = 88–289$ from Liu and O'Neill (2004a; 1.1 GPa), $D^{Cr}_{Sp} = 54$ from Davis et al. (2013; 3 GPa), and $D^{Cr}_{Sp} = 21–761$ from Horn et al. (1994; 1atm) and Wijbrans et al (2015; 1 atm); Fig. 3a). The strong correlation between the D^{Cr}_{Sp} and C^{Cr}_{Sp} is very important, warning that Cr is not as compatible as conventionally thought at Cr-poor conditions. In contrast, other factors such as P, T and f_{O2} may only slightly affect the D^{Cr}_{Sp} values. Cr may show different charge states of 2+, 3+ and 6+ at different f_{O2}, but presumably enters the M-

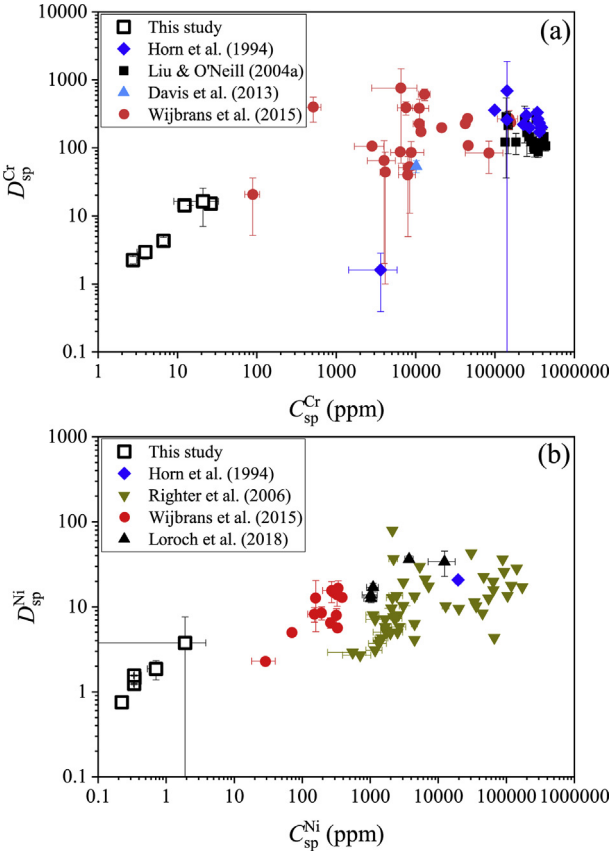

Fig. 3. D^{Cr}_{Sp} vs C^{Cr}_{Sp} (a) and D^{Ni}_{Sp} vs C^{Ni}_{Sp} (b). The plotted spinels from this study, Horn et al. (1994), Wijbrans et al. (2015) and Loroch et al. (2018) are the same as those plotted in Fig. 2. The spinels from Liu and O'Neill (2004a) were synthesized in the CMAS-Cr_2O_3–K_2O system and contained various amounts of Cr_2O_3 (19.5–63.14 wt%; 1.1 GPa and 1320–1380 °C). The spinels from Righter et al. (2006) contained various amounts of Cr_2O_3 (0.11–48.77 wt%) and FeO_t (1.75–66.61 wt%; 1 atm, 1150–1325 °C and $\log f_{O2} = -8.28$ to -0.68). The spinel from Davis et al. (2013) contained some Cr_2O_3 (1.31 wt%) and FeO_t (8.03 wt%; 3 GPa and 1465 °C). Note that the data with $D^{Cr}_{Sp} = 1.6$ from Horn et al. (1994) is likely an outlier, and has been left out of our discussion.

sites of the spinels mainly as Cr^{3+} due to the radius contrasts (0.80, 0.615 and 0.44 Å for Cr^{2+}, Cr^{3+} and Cr^{6+}, respectively; Shannon, 1976). Combing with the very low Cr contents in common silicate melts, whatever the charge state of the Cr is, this results in an insignificant effect of f_{O2} on the D_{Sp}^{Cr}, as observed by Wijbrans et al. (2015). To be practically useful, the following equation, $C_{Melt}^{Cr2O3} = 0.006(0) \times C_{Sp}^{Cr2O3} - 0.005(14)$ ($R^2 = 0.78$; wt%), has been derived from the data shown in Fig. 3a, and describes the Cr_2O_3 distribution between the spinels and silicate melts reasonably well.

Ni The D_{Sp}^{Ni} constrained by our experiments ranges from 0.755 to 3.8(38) (Table 5; averagely 1.8(10)), significantly smaller than the values obtained by other studies at Ni-rich conditions ($D_{Sp}^{Ni} = 20.7(20)$ from Horn et al. (1994), $D_{Sp}^{Ni} = 2.7-79.4$ from Righter et al. (2006), and $D_{Sp}^{Ni} = 2.2-16.7$ from Wijbrans et al. (2015), and $D_{Sp}^{Ni} = 12.6-36.6$ from Loroch et al. (2018); Fig. 3b). The strong correlation between the D_{Sp}^{Ni} and C_{Sp}^{Ni} is very important, warning that Ni is not as compatible as conventionally thought at Ni-poor conditions. In contrast, other factors such as *P*, *T* and f_{O2} may only slightly affect the D_{Sp}^{Ni} values (Wijbrans et al., 2015). Summarily, the data shown in Fig. 3b lead to the following equation, $C_{Melt}^{NiO} = 0.050(2) \times C_{Sp}^{NiO} + 0.009(11)$ ($R^2 = 0.86$; wt%), which may be used to estimate the NiO content of silicate melts.

3.4. Some trace elements and their partitioning between spinels and silicate melts

The abundances of some trace elements in the $MgAl_2O_4$ spinels and the carbonatitic silicate melts, as observed in our high-*P* experiments, and their partition coefficients between these two phases are listed in Table 5.

3.4.1. Phosphorus

No systematic experimental investigation has been carried out to study the partitioning behavior of phosphorus between the spinels and the silicate melts. As a matter of fact, we could find one full analysis only, leading to $D_{Sp}^{P} = 0.06(12)$ at 3 GPa and 1465 °C (Experiment A806; Davis et al., 2013). Phosphorus usually appears as P^{5+}, and its incorporation into the spinel structure thus requires special charge-compensating mechanisms. Further, the effective cation radii of P^{5+} in four-fold coordination and six-fold coordination are respectively ~0.17 and 0.38 Å (Shannon, 1976), and the $d_{T\text{-}O}$ and the $d_{M\text{-}O}$ of the somewhat disordered $MgAl_2O_4$-Sp at magmatic high *T* such as 1100 °C are respectively ~1.9113(7), and 1.9321(4) Å (Andreozzi et al., 2000). Taking the radius of the O^{2-} ion as 1.38 Å (Shannon, 1976), the T-sites and M-sites of the spinel structure are too large for the P^{5+} cation. No significant P^{5+} incorporation is therefore expected. However, our experimentally-determined D_{Sp}^{P} in the *P-T* range of 3–6 GPa and 1500–1650 °C varies from 0.941(7) to 2.22(74) (averagely 1.64(52); Table 5), distinctly different to the value suggested by Davis et al. (2013). To ascertain whether P^{5+} is compatible or incompatible in the spinel structure at high *P*, more experiments are required.

3.4.2. Nb, Ta, Ti, and Sn

The partition coefficients of the high field strength elements (HFSE) Nb, Ta and Ti between the $MgAl_2O_4$-Sp and carbonatitic silicate melts observed in our high-*P* experiments, $D_{Sp}^{Nb} = 3.914-19.08$ (averagely 9.9(65)), $D_{Sp}^{Ta} = 1.74-20.00$ (averagely 8.3(81)) and $D_{Sp}^{Ti} = 0.131-1.205$ (averagely 0.445(396)), are compared with those between the Al ± Cr ± Fe spinels and silicate melts constrained by previous studies in Fig. 4a, b and c, respectively (Horn et al., 1994; Lundstrom et al., 2006; Davis et al., 2013; Wijbrans et al., 2015; Loroch et al., 2018).

Distinctly, the data for the Nb and Ta partition are similarly divided into two groups, a high-*P* group including all the data from this investigation and a 1-atm group including all the data from all previous studies. At similar C_{Sp}^{Nb} (or C_{Sp}^{Ta}), the D_{Sp}^{Nb} (or D_{Sp}^{Ta}) values in the high-*P* group are substantially larger than those in the 1-atm group, by ~5 orders of magnitude. Further, it seems likely that a nominal positive correlation exists between the D_{Sp}^{Nb} (or D_{Sp}^{Ta}) values and the C_{Sp}^{Nb} (or C_{Sp}^{Ta}) values at 1 atm. Since the experimental *P* was all at 1 atm, since a small range of experimental *T* variation at magmatic temperatures should exert negligible influence on the partition coefficients (Jones, 2016), and since some variation of f_{O2} could not significantly affect the partition coefficients (Wijbrans et al., 2015), this nominal positive correlation must be explained by resorting to some compositional variables. As suggested by Wijbrans et al. (2015), substituting of some smaller Al^{3+} by some larger Cr^{3+} and Fe^{3+} in the spinels should expand the M-sites, which usually host the HFSE (the effective cation radius of Al^{3+}, Cr^{3+} and Fe^{3+} in six-fold coordination being respectively ~0.535, 0.615 and 0.645 Å; Shannon, 1976). As a result, larger Nb and Ta cations (both being ~0.68 Å; Shannon, 1976) should more readily enter the M-sites, leading to increasing partition coefficients. Indeed, the spinels from Lundstrom et al. (2006) and Loroch et al. (2018) were all free of Cr^{3+} and Fe^{3+}, those from Wijbrans et al. (2015) contained either no Cr^{3+} ± Fe^{3+} or some Cr^{3+} ± Fe^{3+}, and those from Horn et al. (1994) all contained significant amounts of Cr^{3+} and Fe^{3+}. In correspondence, the Nb (or Ta) partition coefficients at 1 atm increase (Fig. 4a and b). Therefore, the nominal positive correlation exhibited by the Nb (or Ta) partition coefficients at 1 atm does not necessarily mean a breakdown of the Henry's partition law.

If we ignore for a moment the Ti partition data at 3 GPa from Davis et al. (2013) and the data at the C_{Sp}^{Ti} concentrations of a few tens of ppm from Wijbrans et al. (2015) and Loroch et al. (2018), the above discussion on the Nb and Ta partition between the spinels and the silicate melts similarly applies to the Ti partition (Fig. 4c). Nevertheless, Ti is about two orders of magnitude more compatible in the spinels than Nb and Ta at 1 atm (Wijbrans et al., 2015). Using a simulating peridotite + basalt mixture as starting material, the experiment from Davis et al. (2013; Experiment A806) was performed at 3 GPa, with firstly a heating stage of 2 h at 1650 °C, secondly a gradual cooling process of ~31 h to the final *T* (1465 °C), and thirdly a heating phase of 48 h at 1465 °C. The thus-obtained Ti partition coefficient, however, is rather different both to

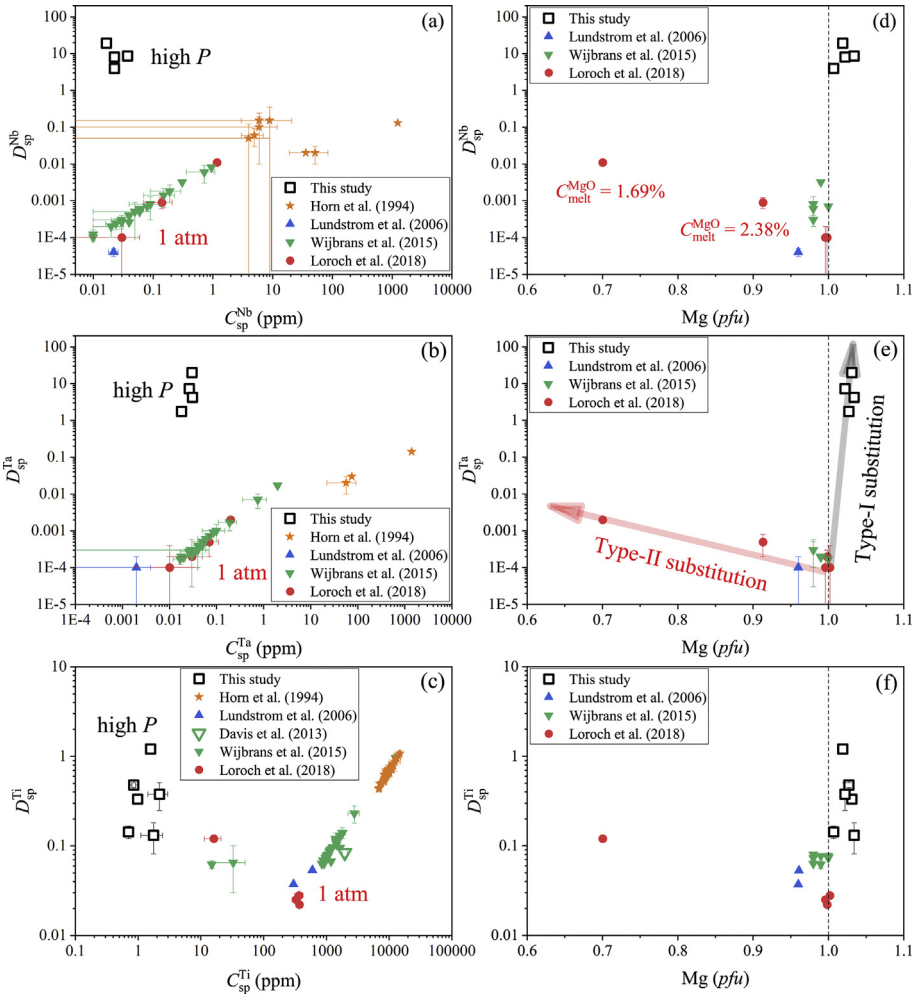

Fig. 4. (a) D_{Sp}^{Nb} vs C_{Sp}^{Nb}, (b) D_{Sp}^{Ta} vs C_{Sp}^{Ta}, (c) D_{Sp}^{Ti} vs C_{Sp}^{Ti}, (d) D_{Sp}^{Nb} vs Mg, (e) D_{Sp}^{Ta} vs Mg, and (f) D_{Sp}^{Ti} vs Mg. In (a), (b) and (c), both the experimental data for spinels containing no Cr and no Fe, and the experimental data for spinels containing Cr ± Fe are plotted. In (d), (e) and (f), only the experimental data for spinels containing no Cr and no Fe are plotted (i.e., Mg−Al spinels in general). *pfu* means per formula unit (on the basis of 4 oxygens in the case of spinel). With the exception of Davis et al. (2013) at 3 GPa, all other investigations in the literature were conducted at 1 atm and with various experimental T and f_{O2}. Note that all Nb and Ta are assumed as 4+ in this study since there are still significant uncertainties on their exact charge states in silicate melts (Burnham et al., 2012; Cartier et al., 2015). For the purpose of clarity, the low C_{Melt}^{MgO} values are only indicated in (d), and the two different substitution mechanisms are only shown in (e), although they are similarly applicable to (e) and (f), and (d) and (f), respectively.

ours at high P in the CMAS-K_2O−CO_2 system, and to those at 1 atm from Horn et al. (1994) in the alkali olivine basalt composition system (Fig. 4c). The reason is not very clear to us at the present. In comparison, the slightly larger D_{Sp}^{Ti} at the C_{Sp}^{Ti} concentrations of a few tens of ppm from Wijbrans et al. (2015) and Loroch et al. (2018) might be partially explained by small amounts of vacancies in the spinels (more later), a mechanism conventionally invoked to interpret negative correlations between the partition coefficients and the low-level concentrations of certain trace element (Harrison and Wood, 1980; Watson, 1985).

To explore the causes to the large differences in the D_{Sp}^{Nb}, D_{Sp}^{Ta}, and D_{Sp}^{Ti} between the high-P group and the 1-atm group, we have plotted all relevant data for the Mg−Al spinels (i.e., both the Cr_2O_3 and Fe_2O_3 contents < 1%) in Fig. 4d, e and f, respectively. Two different mechanisms emerge. For the Mg−Al spinels in the high-P group, their Mg cation is obviously larger than 1, indicating a potential cation substitution reaction like

$$Nb^{4+}\ (Ta^{4+}, \text{ or } Ti^{4+}) + Mg^{2+} = 2Al^{3+} \quad (2)$$

(termed as type-I substitution hereafter). Previously Liu et al. (2018) demonstrated a similar cation substitution reaction for the major elements in the Mg−Al spinels ($Si^{4+} + Mg^{2+} = 2Al^{3+}$). For the Mg−Al spinels in the 1-atm group, their Mg cation number is apparently smaller than 1, suggesting another potential cation substitution reaction like

$$Nb^{4+}\ (Ta^{4+}, \text{ or } Ti^{4+}) + V_{Mg} = 2Mg^{2+} \quad (3)$$

(termed as type-II substitution hereafter), where V_{Mg} stands for charge-balancing vacancies in the Mg^{2+} position of the spinels. As one example, the total cation number in the

Mg–Al spinels with $Mg_{\text{-Sp}} = 0.7$ pfu (per formula unit) was 2.899 pfu only (Run H3-R8 of Loroch et al., 2018), implying a substantial amount of Mg-site defects occurring in the spinel structure.

Although the above two substitution mechanisms regulating the partitioning behavior of Nb, Ta, Ti and potentially other HFSE such as Zr and Hf have been observed via the experimental results acquired respectively at high *P* and at 1 atm, high *P* might not necessarily be the key parameter. The MgO contents of the silicate melts coexisting with the partition coefficient-elevated Mg–Al spinels in the 1-atm experiments were very low, 6.50–7.16 wt% in Lundstrom et al. (2006), 11.7–13.9 wt% in Wijbrans et al. (2015) and 1.69–6.13 wt% in Loroch et al. (2018). For example, the melt phase in that particular experiment H3-R8 of Loroch et al. (2018) just contained 1.69 wt% MgO. In comparison, the MgO contents of the carbonatitic silicate melts in our high-*P* experiments were much higher, varying from ~22.40 to 40.03 wt% (Table 4). We therefore tend to believe that it is the MgO content of the coexisting silicate melts, rather than pressure, to decide which substitution mechanism eventually operates.

The nominally unusual D_{Sp}^{Ti} at 3 GPa from Davis et al. (2013), as discussed above (Fig. 4c), can then be generally explained by a normal MgO content in the silicate melts (~15.0 wt%), neither too high nor too low for the crystallizing of stoichiometric spinels.

The partition coefficients of Sn between the Al–Cr–Fe spinels and silicate melts were not constrained experimentally (Hu et al., 2016). Our high-*P* experiments supply the first few preliminary D_{Sp}^{Sn} values, from ~0.185(19) to 0.44(13) (averagely 0.32(13)), which indicate a general incompatibility for Sn in the $MgAl_2O_4$-spinel structure (Table 5).

3.4.3. U, Th and Pb

Th usually occurs as Th^{4+}, but U and Pb have different charge states at different f_{O2}. When they experimentally studied the trace element partitioning between wollastonite and silicate-carbonate melt (3 GPa, 1420 °C, Pt capsule), Law et al. (2000) assumed that U was 4+, and Pb was 2+ in their experimental product. However, the Pb partition coefficient was much smaller than what was expected for the Pb^{2+} in six-fold coordination, implying at least some of their Pb probably occurring as Pb^{4+}. As our experiments were performed with Pt capsules at similar *P-T* conditions and in a similarly CO_2-rich system, we tend to believe that most U and Pb in our experimental charges were 4+.

The U partition coefficients between some Al–Cr–Fe spinels with various compositions and silicate melts have been experimentally determined at ambient *P*, with D_{Sp}^{U} ranging from 0.000004 to 0.029 (Lundstrom et al., 2006; Wijbrans et al., 2015; Loroch et al., 2018). Although the D_{Sp}^{U} values showed large uncertainty and varied in four orders of magnitude, it is rather clear that U is incompatible in the spinel structure at 1 atm. Our experiments provide preliminary constraints at high *P*, with D_{Sp}^{U} ranging from 0.0773 to 0.6426 (averagely 0.33(25); Table 5), suggesting that U likely remains incompatible in the spinel structure at high *P*. As there is not clear correlation between the D_{Sp}^{U} values and *P* (Fig. 5a), we incline to the idea that a heterovalent substitution mechanism, similar to Eq. (2), functions.

The Th partition coefficients between some Al–Cr–Fe spinels with various compositions and silicate melts have been experimentally determined at ambient *P*, with D_{Sp}^{Th} ranging from 0.00001 to 0.009 (Lundstrom et al., 2006; Wijbrans et al.,

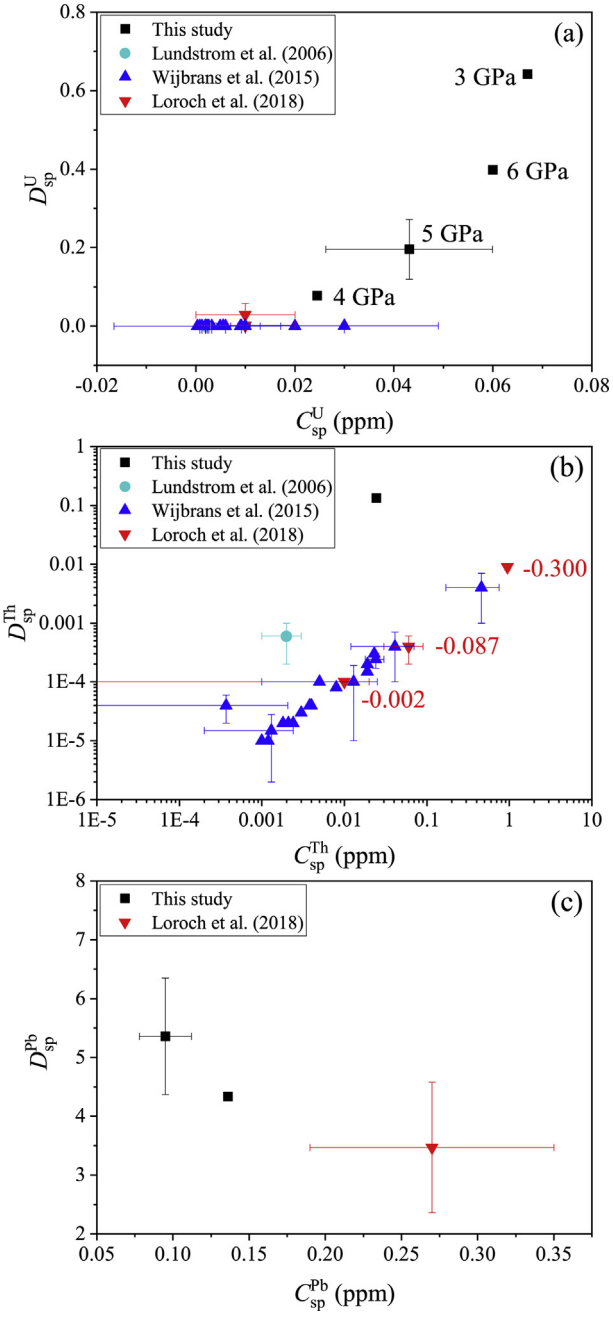

Fig. 5. D_{Sp}^{U} vs C_{Sp}^{U} (a), D_{Sp}^{Th} vs C_{Sp}^{Th} (b), and D_{Sp}^{Pb} vs C_{Sp}^{Pb} (c). The data from this study, Lundstrom et al. (2006) and Loroch et al. (2018) are for the Mg–Al spinels (almost Cr- and Fe-free), and those from Wijbrans et al. (2015) are for the Al–Cr–Fe spinels made in the system CMAS ± FeO ± Cr_2O_3. All previous studies were performed at 1 atm. The Mg shortages (*pfu*) in the Mg–Al spinels from Loroch et al. (2018) shown in (b) are indicated by the numbers along the relevant symbols.

2015; Loroch et al., 2018). Although the D_{Sp}^{Th} values showed large uncertainty and quantitatively varied in two orders of magnitude, it is rather clear that Th is incompatible in the spinel structure at 1 atm. One of our experiments (LMD578) provides preliminary result at 5 GPa and 1630 °C, with D_{Sp}^{Th} = 0.134 (Table 5), suggesting that Th likely remains incompatible at high *P*. In addition, the data from Loroch et al. (2018) show a positive correlation between the D_{Sp}^{Th} and the Mg shortage in the Mg−Al spinels (Fig. 5b), indicating that a heterovalent substitution mechanism, similar to Eq. (3), effects. Further, Fig. 5b shows a nominal positive correlation between the D_{Sp}^{Th} and the C_{Sp}^{Th} data, which has not been well explained by variations of *T*, f_{O2} and spinel composition though (Wijbrans et al., 2015).

The Pb contents in the spinels and silicate melts were usually not analyzed, so that the Pb partitioning between the spinels and the silicate melts has not been well constrained so far. Loroch et al. (2018) once determined the Pb partition coefficient between the Mg−Al spinel and silicate melt as 3.47(111) (Run Mel3-R12 at 1 atm and 1000 °C). Two of our experiments constrain the D_{Sp}^{Pb} values as ~5.36(99) and 4.335 (Table 5). As shown in Fig. 5c, Pb is therefore compatible in the spinel structure at both room *P* and high *P*, which is rather different to the incompatible partitioning behavior of U and Th.

It is rather clear that $D_{Sp}^{Pb} > D_{Sp}^{U} > D_{Sp}^{Th}$ (Fig. 5). For Pb^{4+}, U^{4+} and Th^{4+} in six-fold coordination, their effective radii are 0.775, 0.89, and 0.94 Å, respectively (Shannon, 1976), and all are larger than the cation sites in the spinels. The gradually increasing size difference between these cations and the T-sites and M-sites of the Mg−Al Sp then leads to decreasing partition coefficients (with one to two orders of magnitude difference), as experimentally observed.

It appears that the assumption of all Pb cations occurring as Pb^{2+} in their CO_2-rich experimental charges, made by Law et al. (2000), is not supported by the U, Th, Pb partitioning systematics observed here. Further, the cation radius of Pb^{2+} in six-fold coordination is 1.19 Å (Shannon, 1976), much larger than that of either U^{4+} or Th^{4+} but similar to that of Sr^{2+} in six-fold coordination (1.18 Å; Shannon, 1976). If most Pb were 2+, the D_{Sp}^{Pb} value would have been much similar to the D_{Sp}^{Sr} (significantly < 1; Table 5), which is not the case. Moreover, Liu et al. (2008) and He et al. (2011) synthesized lead apatites via solid−state reaction in open air, with the number of Pb cations always less than the apatite stoichiometry, implying some Pb presenting as Pb^{4+}. More experimental investigation on the relationship between the charge state of Pb and the f_{O2} at both room *P* and high *P* is desirable.

3.4.4. REEs and Y

The partition coefficients of the REEs at 3−6 GPa obtained in this study (Table 5) are D_{Sp}^{La} = 0.001−0.006 (averagely 0.0036(21)), D_{Sp}^{Ce} = 0.003−0.011 (averagely 0.0061(36), D_{Sp}^{Pr} = 0.014−0.065 (averagely 0.044(21)), D_{Sp}^{Nd} = 0.013−0.063 (averagely 0.037(25)), D_{Sp}^{Sm} = 0.111−0.277 (averagely 0.198(82)), D_{Sp}^{Eu} = 0.543 (averagely 0.543), D_{Sp}^{Gd} = 0.115−0.237 (averagely 0.196(70)), D_{Sp}^{Tb} = 0.150−0.312 (averagely 0.215(86)), D_{Sp}^{Dy} = 0.069 (averagely 0.069(10)), D_{Sp}^{Ho} = 0.062−0.166 (averagely 0.108(45)), D_{Sp}^{Er} = 0.374 (averagely 0.374), D_{Sp}^{Tm} = 0.242−1.589 (averagely 0.754(729)), D_{Sp}^{Yb} = 0.267−1.483 (averagely 0.812(440)), and D_{Sp}^{Lu} = 1.557 (averagely 1.557).

These REEs partition coefficients at high *P* are compared in Fig. 6 to those experimentally obtained at 1 atm. Clearly, nearly all REEs are incompatible in the $MgAl_2O_4$-Sp both at high *P* and at 1 atm. Because our experiments were not REEs-doped, however, we could often obtain one or two successful LA-ICP-MS analyses for the REEs in the $MgAl_2O_4$-Sp in every experiment. This leads to relatively low accuracies in the partition coefficients at high *P*. In contrast, the REEs partition coefficients at room *P* were relatively better constrained by the experiments of Lundstrom et al. (2006), Wijbrans et al. (2015) and Loroch et al. (2018). On the basis of the averaged partition coefficients at both 1 atm and high *P*, anyhow, we have obtained a clear positive *P* dependence for the partition coefficient of every REE, as indicated by the red arrows in Fig. 6.

The reason for the positive correlation between the REEs partition coefficients and *P* is not intuitively obvious. The six-fold 3+ REEs have large effective ionic radii (ranging from ~1.032 to 0.861 Å; Shannon, 1976), and could not readily enter the M-sites of the $MgAl_2O_4$-spinel at 1 atm (the $d_{M\text{-}O}$ ranging from ~1.9309 to 1.9321 Å only when *T* changes from 1000 to 1100 °C; Andreozzi et al., 2000), which well explains the incompatible behavior observed at 1 atm by Lundstrom et al. (2006), Wijbrans et al. (2015) and Loroch et al. (2018). High *P* compresses a crystal structure in general, and should have reduced the M-sites of the $MgAl_2O_4$-spinel in particular if nothing unusual took place. Consequently, high *P* would have resulted in diminishing partition coefficients, right opposite to what we have observed in Fig. 6. Two facts might have played important roles in elevating the partition coefficients at high *P*. Firstly, the $MgAl_2O_4$-spinel is much less compressible than the REE metal oxides (Nestola et al., 2007; Jiang et al., 2018), so that the size mismatch between the M-sites and the REE cations should be reduced to some extent by high *P*. Secondly, the $d_{M\text{-}O}$ of the $MgAl_2O_4$-spinel significantly increases due to the Mg−Al cation disordering process (Redfern et al., 1999; Andreozzi et al., 2000), which is substantially enhanced by high *P* (Da Rocha and Thibaudeau, 2003; Méducin et al., 2004). The size mismatch between the M-sites and the REE cations should be further reduced hence.

Another important feature shown in Fig. 6 is that at high *P* the partition coefficients of some REEs (those for the heavy REEs such as Tm, Yb and Lu) might become larger than 1 whereas the partition coefficients of others (such as those for the light REEs La, Ce, Pr, and etc.) may remain much smaller than 1. Therefore, the crystallization of spinels from magmas at high *P* has the potential to fractionate the REEs, a phenomenon which has been conventionally attributed to the crystallization of garnets. This potential role can be better illustrated with Fig. 7.

The D_{Sp}^{Y} varies from 0.0004 to 0.009 (averagely 0.0051(36); Table 5), so that Y is incompatible in the spinel structure, in good agreement with Loroch et al. (2018).

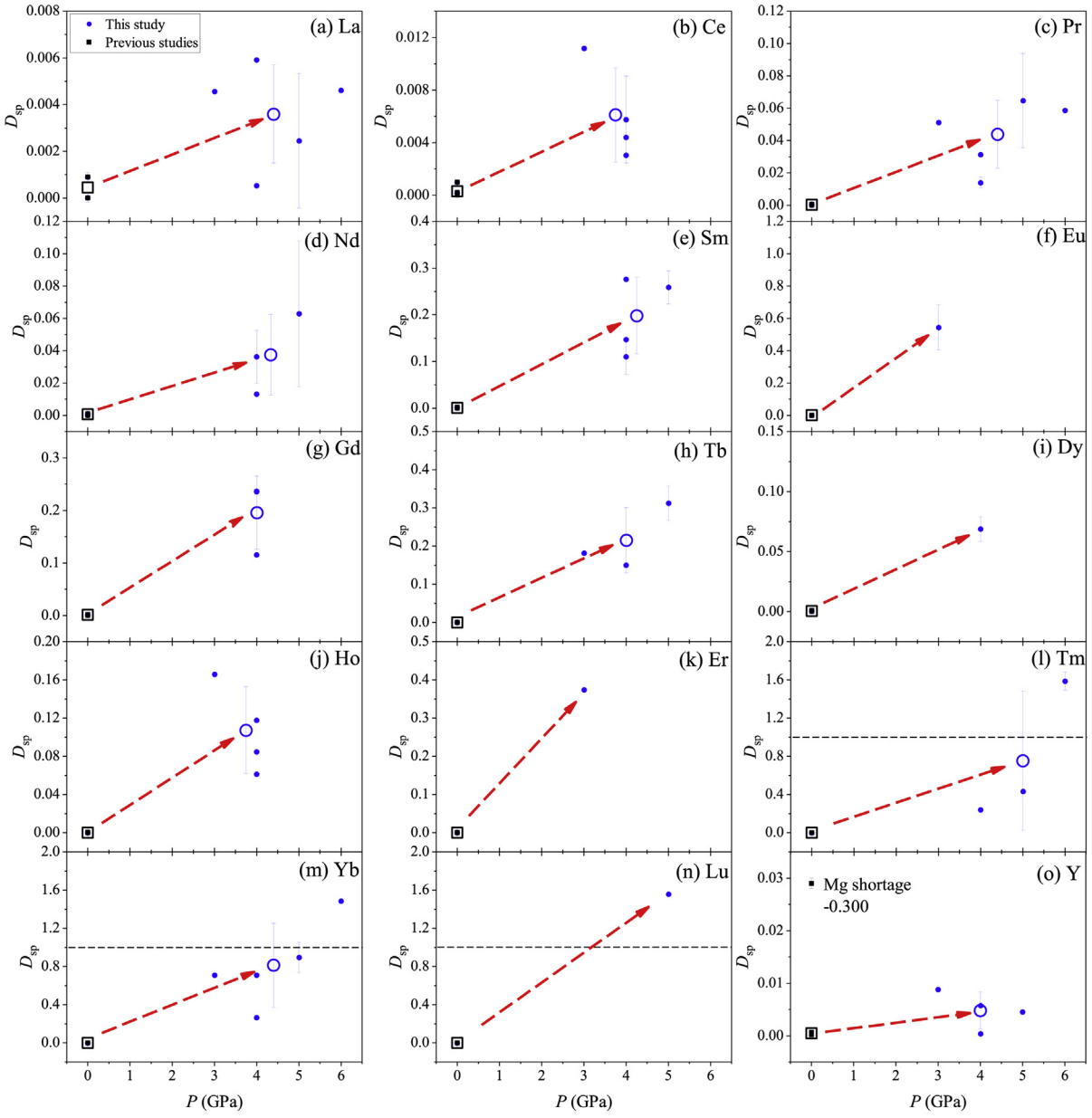

Fig. 6. Effect of P on the REEs and Y partition: (a) La; (b) Ce; (c) Pr; (d) Nd; (e) Sm; (f) Eu; (g) Gd; (h) Tb; (i) Dy; (j) Ho; (k) Er; (l) Tm; (m) Yb; (n) Lu; (o) Y. The coefficients for the REEs partitioning between the $MgAl_2O_4$-Sp and melt at 1 atm are from Lundstrom et al. (2006), Wijbrans et al. (2015) and Loroch et al. (2018), and those at high P are from this study. All experimental determinations are represented by small symbols, either filled squares (1 atm) or circles (high P). Due to the data availability and accuracy limit, the experimental determinations have been grouped according to their experimental P and then averaged, with the averages for 1 atm and high P shown as large empty squires and circles, respectively. In order to show the effects of P (represented by the red arrows), we have chosen to ignore any effects of T (1000−1350 °C at 1 atm vs 1500−1650 °C at high P) and melt composition (silicate melts at 1 atm vs carbonatitic silicate melts at high P).

3.4.5. Mn and Fe

The partition coefficients of Mn and Fe between the $MgAl_2O_4$-Sp and carbonatitic silicate melts observed in our high-P experiments, D_{Sp}^{Mn} = 0.71−3.14 (averagely 1.9(11)), D_{Sp}^{Fe56} = 2.9−11.2 (averagely 7.9(3.0)), are compared with those between the Al ± Cr ± Fe spinels and silicate melts constrained by previous studies in Fig. 8a and b, respectively (Horn et al., 1994; Mallmann and O'Neill, 2009; Davis et al., 2013; Wijbrans et al., 2015).

As shown in Fig. 8a, there is no obvious trend defined by the D_{Sp}^{Mn} and C_{Sp}^{Mn}. Our determinations, indicating no P dependence, were likely affected by the low Mn contents in our experiments, with the results from LMD563 being the most reliable ones (Table 5; D_{Sp}^{Mn} = 0.72(28) at 4 GPa and 1550 °C). In contrast, the determinations from Horn et al. (1994) were likely affected by the high Mn contents. It follows that Mn is slightly incompatible in the spinel structure (Fig. 8a). Further, this incompatible partition behavior is

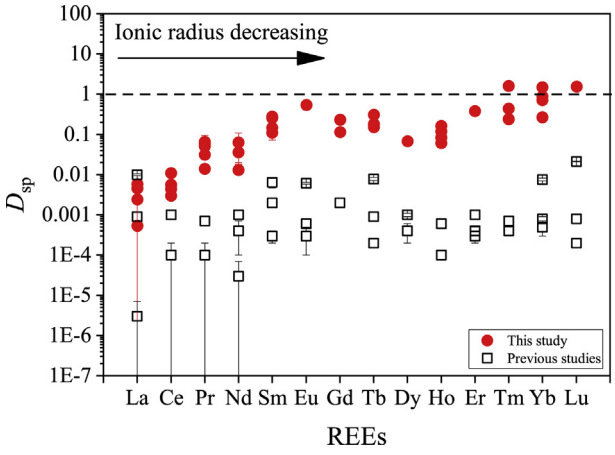

Fig. 7. Variation of D_{Sp}^{REE} with REEs ion radius at high P and 1 atm. The data at high P are from this study, and those at 1 atm are from Nagasawa et al. (1980), Lundstrom et al. (2006), and Loroch et al. (2018).

unlikely strongly affected by the variables P, T, f_{O2}, and certain compositions (such as Cr, Fe, C, and etc.), in consistent with the conclusion drawn by Wijbrans et al. (2015). At C_{Sp}^{Mn} > ~0.1%, the Henry's law behavior may break down (Fig. 8a).

Our data suggest that Fe is compatible in the $MgAl_2O_4$-Sp (Fig. 8b). They further suggest that P does not affect this compatibility. In comparison, the D_{Sp}^{Fe} seems to be influenced by f_{O2}, increasing with increasing f_{O2}, as indicated by the 1-atm data from Mallmann and O'Neill (2009; Fig. 8b). This observation is likely supported by the 1-atm data from Wijbrans et al. (2015) and Horn et al. (1994), with the f_{O2} and D_{Sp}^{Fe} values in the latter collectively higher than those in the former. Difference in the f_{O2} values in the high-P experiments from this study and from Davis et al. (2013) may also explain the difference in the D_{Sp}^{Fe} values at high P. At C_{Sp}^{Fe} > ~10%, the Henry's law behavior may break down (Fig. 8b).

Moreover, Fe naturally occurs as a range of stable isotopes in different abundances, 5.8 mol% Fe^{54}, 91.75 mol% Fe^{56}, 2.1 mol% Fe^{57} and 0.28 mol% Fe^{58} (Taylor et al., 1992). The fractionation of the Fe isotopes at high P-T conditions may have important geological implications (Polyakov, 2009; Liu J et al., 2016). It has been shown that there are substantial systematic variations in the Fe isotope compositions (e.g., $Fe^{57/54}$) of mantle spinels (Williams et al., 2004). Here we have obtained some preliminary results for the Fe^{56} and Fe^{57} partitioning between the $MgAl_2O_4$-Sp and carbonatitic silicate melts. The D_{Sp}^{Fe57} values range from ~0.593 to 2.227 (averagely 1.4(8); Table 5), are thus much smaller than the D_{Sp}^{Fe56}, suggesting an $Fe^{57/56}$ isotope fractionation.

3.4.6. Sr and Ba

The cation radii of Sr^{2+} and Ba^{2+} in six-fold coordination are respectively 1.18, and 1.35 Å (Shannon, 1976), and thus too large for the T-sites or M-sites of the spinels. They are hence expected to be incompatible in the spinel structure. The partition coefficients of Sr and Ba between the $MgAl_2O_4$-spinel and the silicate melt determined in our high-P experiments are respectively ~0.0004–0.004 (averagely 0.0015(12)) and 0.010–0.023 (averagely 0.015(6); Table 5). In comparison, they were respectively constrained as ~0.002–0.024 and 0.003–0.029 by the 1 atm experiments of Loroch et al. (2018). These two elements are thus incompatible in the $MgAl_2O_4$-spinel indeed. P and composition of the silicate melts (distinctly, carbon-rich silicate melts in this study vs carbon-free silicate melts in Loroch et al., 2018) have insignificant influence on this incompatibility.

The data are summarized in Fig. 9. Indeed, no clear correlation between the D_{Sp}^{Sr} (or D_{Sp}^{Ba}) and P can be observed. However, Fig. 9 shows that there appears to be a positive correlation between the D_{Sp}^{Sr} (or D_{Sp}^{Ba}) and the Mg cation shortage in the $MgAl_2O_4$-spinel, mainly suggested by the data

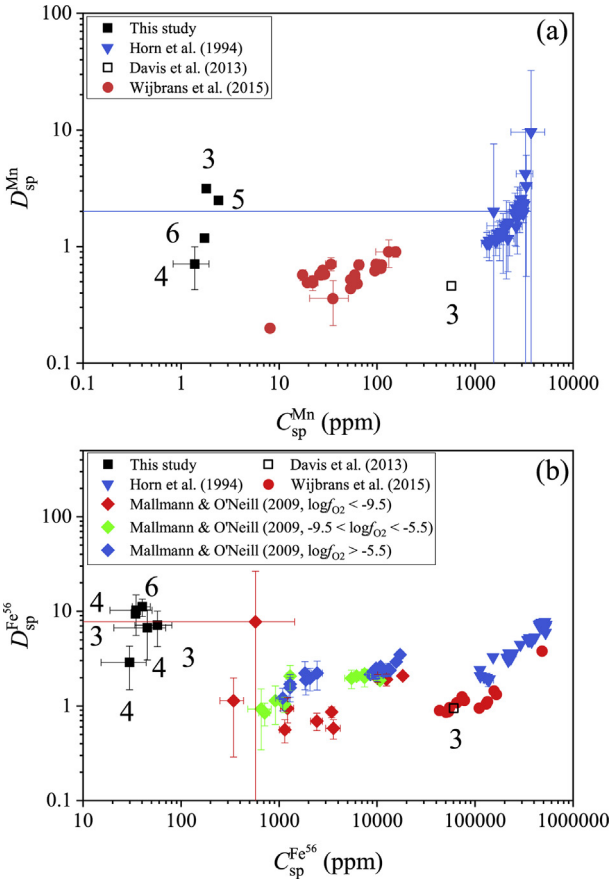

Fig. 8. (a) D_{Sp}^{Mn} vs C_{Sp}^{Mn} and (b) D_{Sp}^{Fe} vs C_{Sp}^{Fe}. The data from this study (3–6 GPa) and from Davis et al. (2013; Run A806 at 3 GPa) are for high P, and those from other studies are for 1 atm. Note that the experiments from Horn et al. (1994) were carried out with a natural alkali olivine basalt under different oxygen fugacities (log f_{O2} = −8.28 to −0.68), the experiments from Mallmann and O'Neill (2009) were performed in the system CMAS doped with small amounts of P_2O_5, TiO_2, V_2O_5, Cr_2O_3 and Fe_2O_3 (the experiments arbitrarily divided into three groups, those with log f_{O2} < −9.5, those with log f_{O2} = −9.5 to −5.5, and those with log f_{O2} > −5.5), the experiment from Davis et al. (2013) was conducted with a peridotite + basalt mixture at 3 GPa and 1465 °C (inner graphite crucible in outer Pt capsule), and the experiments from Wijbrans et al. (2015) were made in the system CMAS ± FeO ± Cr_2O_3 (log f_{O2} = −12 to −0.7). The D_{Sp}^{Fe} and C_{Sp}^{Fe} data from our study are for Fe^{56} only whereas those from other studies are for Fe^{56} + Fe^{57}. The numbers along some of the symbols are experimental P in GPa.

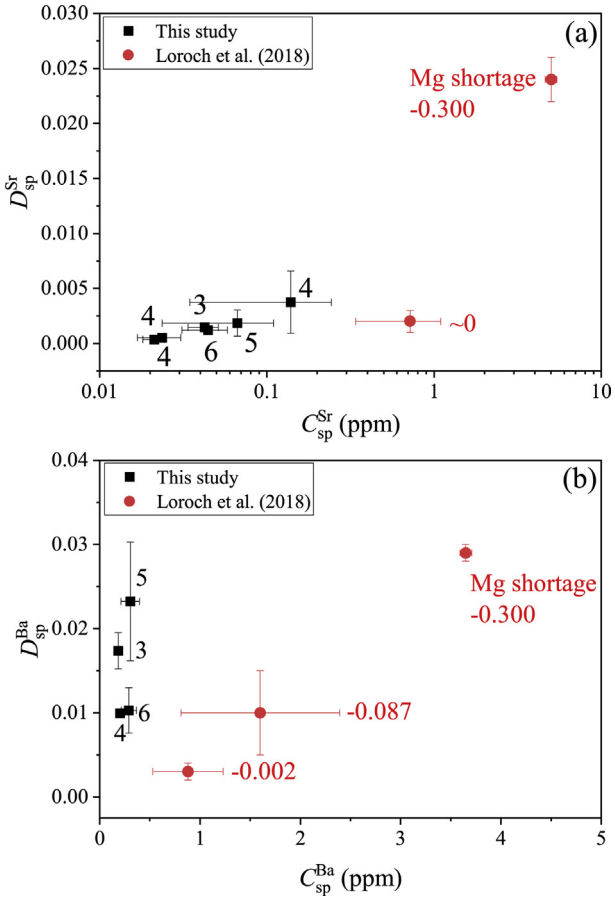

Fig. 9. (a) D^{Sr}_{Sp} vs C^{Sr}_{Sp} and (b) D^{Ba}_{Sp} vs C^{Ba}_{Sp} of $MgAl_2O_4$-spinel. Note that there is no clear correlation between the D^{Sr}_{Sp} (or D^{Ba}_{Sp}) and *P*, but there is likely a positive correlation between the D^{Sr}_{Sp} (or D^{Ba}_{Sp}) and the Mg shortage (*pfu*) of the $MgAl_2O_4$-spinel at 1 atm. The Mg shortages in the $MgAl_2O_4$-spinel from Loroch et al. (2018) are indicated by the numbers along the relevant symbols.

of Loroch et al. (2018). We thus propose that the Sr (Ba) abundance in the $MgAl_2O_4$-spinel increases to some extents due to the volumetric expansion caused by the creation of Mg vacancy, leading to elevated partition coefficients in the end. In contrast, the fluctuation of the D^{Sr}_{Sp} (or D^{Ba}_{Sp}) for the generally stoichiometric $MgAl_2O_4$-spinel at high *P* cannot be readily explained. Presumably, this phenomenon is related to the both *P*-dependent and *T*-dependent Mg−Al cation disordering process (Da Rocha and Thibaudeau, 2003; Méducin et al., 2004).

3.4.7. Na, K and Rb

The partition coefficients of Na, K and Rb determined in our high-*P* experiments are respectively ~0.01−0.042, 0.000−0.004, and 0.047−0.179 (Table 5). These elements are thus incompatible in the $MgAl_2O_4$-spinel. This is presumably partially because of their 1+ charge state, and partially because of their much larger sizes relative to the T-sites and M-sites of the $MgAl_2O_4$-spinel. For the former, some vacancies or other cations with suitable charges are required to accompany the Na, K and Rb incorporation, in order to maintain an electric neutrality. For the latter, the effective ionic radii of the four-fold Na^{1+} and K^{1+} are respectively 0.99 and 1.37 Å, and those of the six-fold Na^{1+}, K^{1+} and Rb^{1+} are respectively 1.02, 1.38 and 1.52 Å (Shannon, 1976). However, the $d_{T\text{-}O}$ and the $d_{M\text{-}O}$ of the somewhat disordered $MgAl_2O_4$-spinel at high *T* such as ~1000−1100 °C are respectively from ~1.9141 to 1.9113 Å, and from ~1.9309 to 1.9321 Å only (Andreozzi et al., 2000). Taking the radius of the O^{2-} ion as 1.38 Å (Shannon, 1976), the mean sizes of the T-sites and M-sites of the $MgAl_2O_4$- spinel should be too small to host any significant amounts of Na, K and Rb.

Fig. 10a, b and c summarize our data and those of Loroch et al. (2018) from the simple composition system, along with the data of Horn et al. (1994) and Davis et al. (2013) from some more complex composition systems (containing Cr_2O_3, Fe_2O_3, and etc.). The good trends defined by these data obtained at different *P* and *T* conditions in different composition systems suggest that the variables *P*, *T*, and certain compositions do not have significant effects on the partitioning behavior of Na, K and Rb. As might be expected from the volumetric expansion when larger Cr^{3+} and Fe^{3+} replace smaller Al^{3+} in the $MgAl_2O_4$-spinel structure, the partition coefficients would increase somewhat, which however is not clearly defined in Fig. 10d and e. Nevertheless, Fig. 10a, b and c show that as the ionic radius increases from Na to Rb, the abundances of Na, K and Rb in the spinels likely decrease, nominally in agreement with the expectation.

More interestingly, Fig. 10 shows two unusual features for the Na, K and Rb partitioning between the spinels and melts. Firstly, the partition coefficients of K are overall smaller than those of Na by about one order of magnitude, which can be explained by the size difference, but the partition coefficients of Rb are surprisingly larger than those of Na by about one order of magnitude, which is at odd and needs further experimental investigation. Nevertheless, the much larger D^{Rb}_{Sp} values are defined by the data from Loroch et al. (2018) only, and they presumably positively correlate with the Mg shortages in the Mg−Al spinels (Fig. 10c). Secondly, Fig. 10 shows that the partition coefficients of Na, K and Rb are all dependent on their abundances in the spinels (in the melts as well), implying potential non-Henry's law behavior. Although non-Henry's law behavior was observed for some trace elements in the silicate systems before (Harrison and Wood, 1980; Bindeman and Davis, 2000), it has been generally accepted by the scientific community that Henry's law is usually satisfied over a wide range of trace element concentrations, up to wt% doping levels (Watson, 1985; Beattie, 1993). Further experimental investigation on the partitioning behavior of Na, K and Rb between the spinels and the silicate melts is deemed necessary.

3.5. Trace elements and their partitioning between Ol/Grt and silicate melts

The abundances of the trace elements in the Ol/Grt, and their partition coefficients between the Ol/Grt and the carbonatitic silicate melts determined in our high-*P* experiments are listed in Table 6 (see Table 5 for the relevant melt

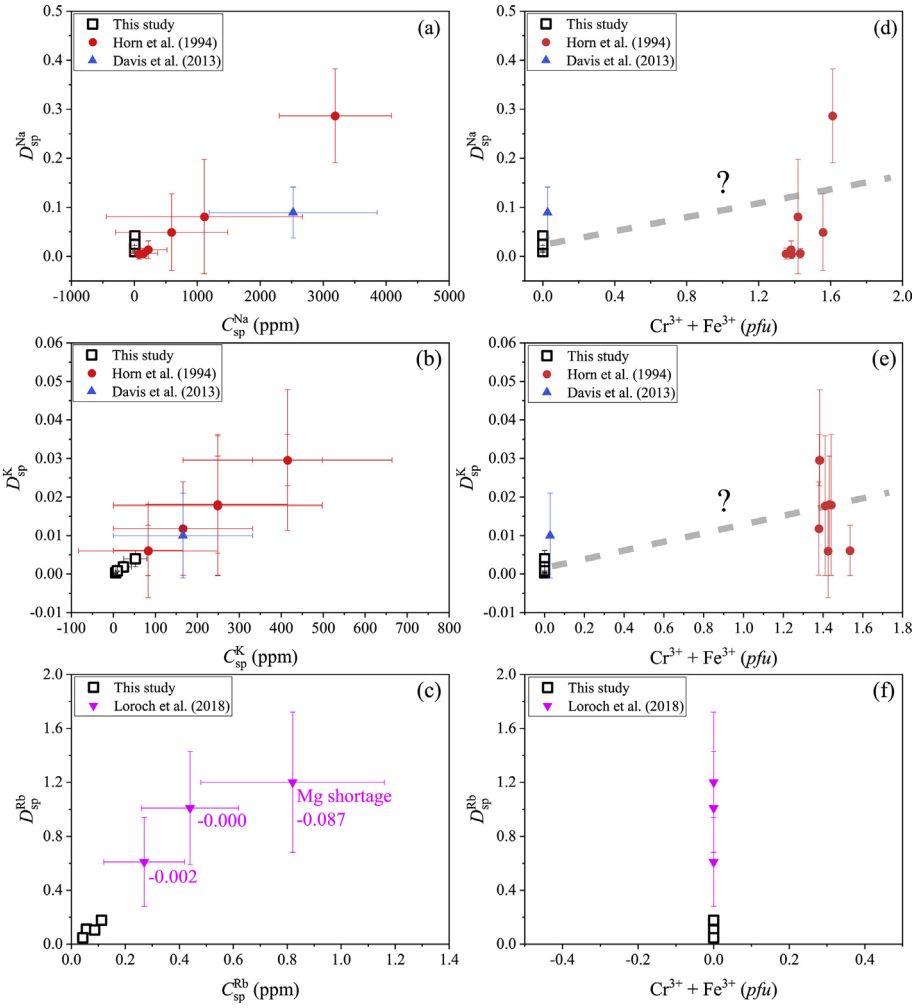

Fig. 10. (a) D^{Na}_{Sp} vs C^{Na}_{Sp}, (b) D^{K}_{Sp} vs C^{K}_{Sp}, (c) D^{Rb}_{Sp} vs C^{Rb}_{Sp}, (d) D^{Na}_{Sp} vs ($Cr^{3+} + Fe^{3+}$), (e) D^{K}_{Sp} vs ($Cr^{3+} + Fe^{3+}$), and (f) D^{Rb}_{Sp} vs ($Cr^{3+} + Fe^{3+}$) of spinels. This study and Davis et al. (2013) were performed at high P (3–6 GPa, and 3 GPa, respectively), and Horn et al. (1994) and Loroch et al. (2018) were done at 1 atm. The experiments from Horn et al. (1994) were carried out with a natural alkali olivine basalt (1 atm; 1235–1340 °C; logf_{O2} = −8.28 to −0.68), and the experiment from Davis et al. (2013) was conducted with a peridotite + basalt mixture (3 GPa; 1465 °C; inner graphite crucible in outer Pt capsule); these experiments thus generated Al–Cr–Fe spinels. In comparison, the experiments from Loroch et al. (2018) and from this study produced $MgAl_2O_4$-spinel (i.e., without significant Fe^{3+} and Cr^{3+}). *pfu* means per formula unit (on the basis of 4 oxygens in the case of spinel). Note that some of the $MgAl_2O_4$-spinels from Loroch et al. (2018) were not strictly stoichiometric, as indicated by the Mg shortage (*pfu*; numbers along the relevant symbols in (c)).

compositions). A brief comparison on the REEs partitioning behaviors observed here and in some previous experimental investigations is shown in Fig. 11. Indeed, Grt is capable of fractionating the REEs whether the composition system is C-bearing (this study) or C-free (other studies), with this capability somewhat enhanced by higher P. In comparison, Ol does not take much REEs, in good agreement with Salters et al. (2002) and Imai et al. (2012).

4. Implications

Partitioning of trace elements between minerals and silicate melts is dependent on many factors such as T, P, composition and oxygen fugacity. In the case of the magmatic Al–Cr–Fe spinel, one of the primary phases possibly crystallizing from silicate magmas at high P, most previous studies on its trace element partitioning behavior were conducted at 1 atm (e.g., Nagasawa et al., 1980; Lundstrom et al., 2006; Loroch et al., 2018). At high P, Davis et al. (2013) presented the only experiment (Run A806; 3 GPa and 1465 °C) which constrained the partition coefficients for a few trace elements (e.g., D^{Sc}_{Sp} = 0.058(8), D^{Ti}_{Sp} = 0.084(8), D^{V}_{Sp} = 2.75(19), D^{Cr}_{Sp} = 54(11), D^{Mn}_{Sp} = 0.46(3), D^{Fe}_{Sp} = 0.95(6), D^{Co}_{Sp} = 3.0(6), D^{Zn}_{Sp} = 5.2(5), D^{Ga}_{Sp} = 6.5(5) and D^{Ge}_{Sp} = 0.40(4)). The high-P partitioning systematics of the trace elements between the Al–Cr–Fe spinels and the silicate magmas are thus inadequately experimentally constrained and poorly understood. Our results here obtained at high P should then have important implications on the evolution of the trace elements in the magmatic process deep in the Earth.

Let us focus on the REEs partition behavior.

As shown in Fig. 12a, the averaged REEs partition coefficients at 1 atm are mostly less than 0.001 and almost constant for all REEs, suggesting a negligible role of the

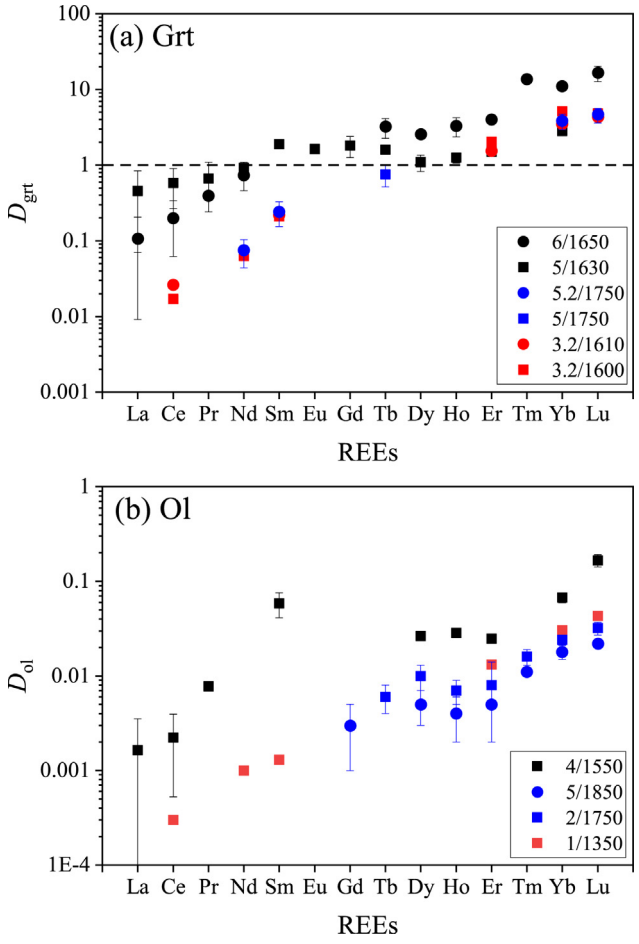

Fig. 11. Comparisons of D_{Grt}^{REE} (a) and D_{Ol}^{REE} (b). The data from this study are shown as black symbols, those from Salters et al. (2002; Experiments RD1097-4 and RD1097-5 for Grt, and experiment TM0500-3 for Ol) as red symbols, those from Draper et al. (2003; Experiments 243 and 190 for Grt) and from Imai et al. (2012; Experiments P775 and S1606 for Ol) as blue symbols. The experiments from Salters et al. (2002; ~5.9 wt% FeO in Grt and ~11.8 wt% FeO in Ol) and Imai et al. (2012; ~3.95–5.55 wt% FeO in Ol) were carried out with peridotitic bulk compositions, and those from Draper et al. (2003; ~12.24–14.92 wt% FeO in Grt) were performed with a chondritic bulk composition. Note that the P (GPa) and T (°C) conditions of the experiments are indicated by the numbers along the symbols.

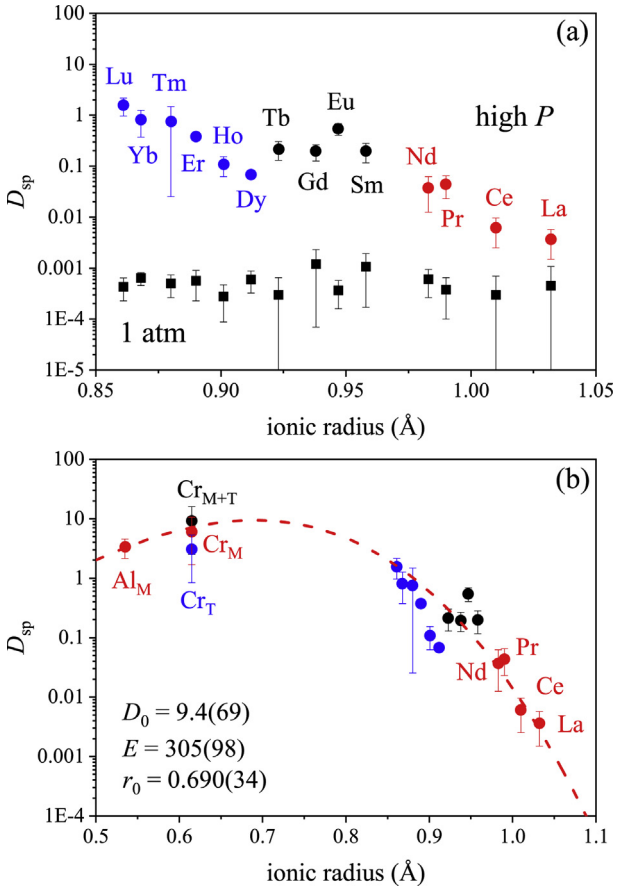

Fig. 12. (a) Comparison of averaged REEs partition coefficients at 1 atm and high P; (b) Averages of partition coefficients of 3+ cations at high P vs cation radius. The data used to derive the averages at high P are from this study, and those used to derive the averages at 1 atm are from Nagasawa et al. (1980), Lundstrom et al. (2006) and Loroch et al. (2018). All Eu cations are assumed as 3+. According to Méducin et al. (2004) and Liu et al. (2018), the Al cations in the $MgAl_2O_4$-spinel from our high-P experiments should be almost randomly distributed on the M-sites and T-sites, so that $D_{Sp}^{Al_M} = 0.667 \times D_{Sp}^{Al_{M+T}}$ and $D_{Sp}^{Al_T} = 0.333 \times D_{Sp}^{Al_{M+T}}$, with $D_{Sp}^{Al_M}$, $D_{Sp}^{Al_T}$ and $D_{Sp}^{Al_{M+T}}$ standing for the M-sites Al partition coefficient, the T-sites Al partition coefficient, and the total Al partition coefficient, respectively. Based on our unreported preliminary data on the $MgCr_2O_4$-spinel synthesized at similar P-T conditions, we assume that the trace Cr cations are also generally randomly distributed on the M-sites and T-sites, so that $D_{Sp}^{Cr_M} = 0.667 \times D_{Sp}^{Cr_{M+T}}$ and $D_{Sp}^{Cr_T} = 0.333 \times D_{Sp}^{Cr_{M+T}}$. With T fixed as 1563 °C (averaged T of all our experimental T), we fit the averaged $D_{Sp}^{Al_M}$, $D_{Sp}^{Cr_M}$, D_{Sp}^{Nd}, D_{Sp}^{Pr}, D_{Sp}^{Ce} and D_{Sp}^{La} to Eq. (4), with the result shown as the red broken curve in (b).

spinels in incorporating and fractionating the REEs. This phenomenon can be easily explained by the combined effects of the cation disordering process and the thermal expansion of the spinels. In a somewhat larger magmatic T range of 1000–1400 °C (mostly decided by bulk composition and P), and taking the $MgAl_2O_4$-spinel as an example, the x values slightly change from ~0.27 at 1000 °C to ~0.36 at 1400 °C, leading to corresponding variations in the $d_{M\text{-}O}$ from ~1.9309 to 1.9383 Å, and in the $d_{T\text{-}O}$ from 1.9139 to 1.8983 Å, according to Andreozzi et al. (2000). Additionally, the thermal expansion in this T range can only slightly increase the $d_{M\text{-}O}$ and $d_{T\text{-}O}$, by less than 0.01 Å (Redfern et al., 1999; Andreozzi et al., 2000). In comparison, the REE–O bond lengths are much longer, changing from 2.241 (Lu–O) to 2.412 Å (La–O), if we ignore any T effect. Consequently, all REEs cannot readily enter either the M-sites or the T-sites, and they must behave incompatibly and show little fractionation during the $MgAl_2O_4$-spinel crystallization from the magmas. Further, substitution of smaller Al^{3+} by larger Cr^{3+} and Fe^{3+} can enlarge the M-sites and T-sites to some extents (Hill et al., 1979), but the size dilatations (mostly less than 0.1 Å) are not large enough to bring forth any significant difference in the REEs partitioning behavior at 1 atm, right as observed in those early experimental studies (Fig. 12a).

At high P as those covered by our experiments, the partitioning behavior of the REEs between the spinels and the silicate melts are fundamentally different (Fig. 12a), with

some D_{Sp} values becoming larger than 1 (e.g., $D_{Sp}^{Lu} = 1.557$) and the D_{Sp} values showing significant variation (e.g., $D_{Sp}^{Lu}/D_{Sp}^{La} = 433$, as compared to $D_{Sp}^{Lu}/D_{Sp}^{La} = 3.5$ at 1 atm by Nagasawa et al. (1980)). These distinct differences were ambiguously attributed to high P in our previous discussion. However, the spinel oxides have a tough structure, expanding little at high T and contracting little at high P (Andreozzi et al., 2000; Nestola et al., 2007; Wang et al., 2012; Liu X et al., 2016; Zhang et al., 2016; Mi et al., 2018), with these effects largely canceling each other out at simultaneous high P-T conditions (Méducin et al., 2004). Other factors must be sought then. According to Méducin et al. (2004), the x values of the $MgAl_2O_4$-spinel in our high-P experiments should be close to 0.667 (Liu et al., 2018). If we extrapolate the experimental results of Andreozzi et al. (2000) to $x = 0.667$ (room P and T), we obtain $d_{M\text{-}O} = 1.9644$ Å and $d_{T\text{-}O} = 1.8445$ Å. These extrapolated results are significant in two respects: firstly, the $d_{M\text{-}O}$ now is much larger than its values at 1 atm (e.g., ~1.9309 to 1.9383 Å as T varies from 1000 to 1400 °C), so that the M-sites become more accommodating to the REEs; secondly, the relative difference between the $d_{M\text{-}O}$ and $d_{T\text{-}O}$ now is much larger as well (~6.5%, compared to ~0.9% at 1000 °C and ~2.1% at 1400 °C under 1 atm), so that the M-sites and T-sites may be able to host different REEs and eventually fractionate them. The larger compressibility of the REEs, compared to the toughness of the spinel structure, should reduce the REEs much more at high P, and thus facilitate the REEs incorporation in the spinels further.

It follows that the REEs partition coefficients between the spinels and the silicate melts at certain P and T may roughly fall into three groups, with those large REEs mainly residing on the M-sites forming one group, those small REEs mainly docking at the T-sites forming another group, and those intermediately-sized REEs appearing on both the M-sites and the T-sites forming another group. This is likely observed in this study (Fig. 12a), with large La, Ce, Pr and Nd mainly residing on the M-sites (red circles), small Lu, Yb, Tm, Er, Ho, and Dy on the T-sites (blue circles), and the left Tb, Gd, Eu and Sm perhaps on both types of sites (black circles).

Consequently, we have tentatively fitted the averaged high-P partition coefficients of those elements (Mg, Al, Cr, La, Ce, Pr and Nd) expected to appear on the M-sites to the lattice strain model (Brice, 1975; Blundy and Wood, 1994),

$$D_i = D_o \exp\left(\frac{-4\pi E_M N_A \left(\frac{r_0}{2}(r_i - r_0)^2 + \frac{1}{3}(r_i - r_0)^3\right)}{RT}\right) \quad (4)$$

where D_i is the partition coefficient of element i with ionic radius r_i, r_0 is the optimum radius calculated for a hypothetical cation which enters the M-sites without any strain, D_0 is the corresponding optimum partition coefficient of this hypothetical cation, N_A is the Avogadro's number, E_M is the Young's modulus of the M-sites, R is the gas constant and T is in K. The result is shown as the red broken curve in Fig. 12b. Obviously, the fitting appears much reasonable, with $r_0 = 0.690(34)$ Å laying between the sizes of the six-fold coordinated Mg and Al cations (0.720 and 0.535 Å respectively; Shannon, 1976). Assuming the M-sites behaves as perfect Poisson's solids (Blundy and Wood, 1994), the derived Young's modulus of the M-sites, 305(98) GPa, should lead to a polyhedral bulk modulus of ~203 GPa, which also lays between the polyhedral bulk moduli of the MgO_6 and AlO_6 (161(5) and 240(20) GPa, respectively; Hazen and Finger, 1979). It hence appears that our assignment of all large La, Ce, Pr and Nd cations to the M-sites is likely correct.

We could have similarly fitted our experimentally-determined partition coefficients of those elements on the T-sites to Eq. (4) if there were radius data for the REEs in four-fold coordination (Shannon, 1976). As shown in Fig. 12b, the small REEs such as Lu, Yb, Tm, Er, Ho, and Dy have partition coefficients smaller than the values predicted for their appearing on the M-sites (the red broken curve), implying their predominant presence on the T-sites. In comparison, the partition coefficients of the intermediate REEs such as Tb, Gd, Eu and Sm are larger than the values predicted for their appearing just on the M-sites, potentially implying their presence both on the M-sites and on the T-sites.

It has to be concluded that the order-disorder process of the cations in the spinels, distinct at high P, can fundamentally modify the partitioning behavior of the REEs between the spinels and the silicate melts. This conclusion should be similarly applicable to the partitioning behavior of other trace elements.

The significance of the cation disorder at high P-T conditions on the trace element partitioning may be quantitatively assessed, as shown for the $MgAl_2O_4$-spinel in Fig. 13. Let us take the condition of $P = 1$ atm, $T = -273$ °C and $x = 0$ as the reference condition. Without triggering any Mg−Al cation disordering (Fig. 13a), the sizes of the T-sites and the M-sites respectively expand by ~2.99% and 4.08%, and by ~3.94% and 5.36%, as T increases from −273 to 1000 and to 1400 °C at 1 atm. P increase suppresses these site dilatations to some extents; for examples, the T-sites and M-sites expansions relative to the reference condition become ~1.39% and 2.36% at 3 GPa, and −0.21% and 0.63% at 6 GPa when $T = 1000$ °C, and become ~2.33% and 3.64% at 3 GPa, and 0.73% and 1.92% at 6 GPa when $T = 1400$ °C. There are even P-T conditions, with the effect of T on the sizes of the T-sites or M-sites being fully counteracted by the effect of P (the solid lines in Fig. 13a). The combined effects of P and T are thus limited, which are in sharp contrast to the large effects of the Mg−Al cation exchange reaction shown in Fig. 13b. Let us take the condition of $P = 1$ atm and $T = 25$ °C as the reference condition. The experimental results from Andreozzi et al. (2000), with some extrapolations to both smaller x and larger x, show that the sizes of the T-sites and the M-sites not only vary significantly in their absolute values ($d_{T\text{-}O}$ and $d_{M\text{-}O}$ indicated by the solid lines with broken extensions), but also vary significantly in their relative magnitudes (the numbers along the square symbols). As x increases from 0 to 0.667, the sizes of the T-sites and the M-sites decrease by 20.34%, but increase by 10.63%, respectively. These values are distinctly larger

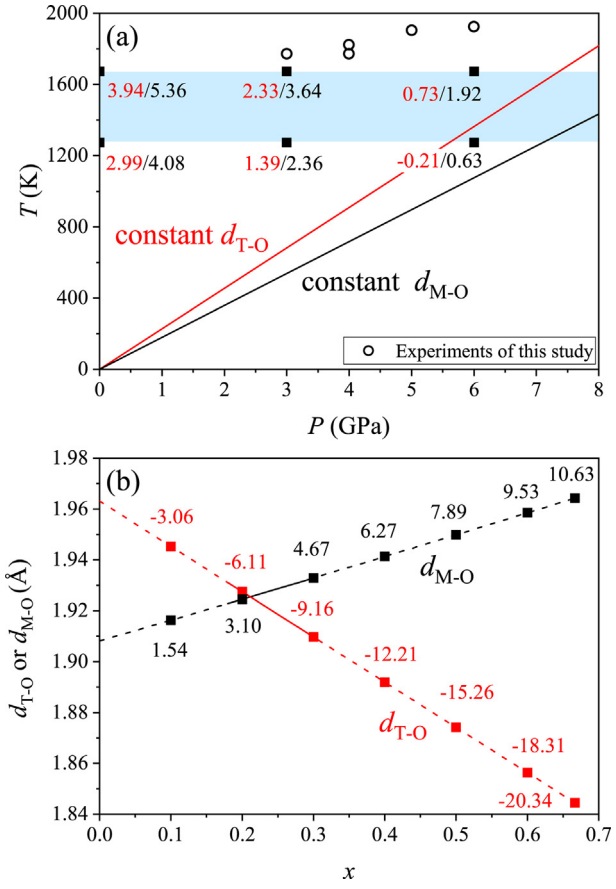

Fig. 13. Significance of Mg–Al cation exchange reaction on the T-sites and M-sites of the $MgAl_2O_4$-Sp: (a) Effects of P and T on the sizes of the T-sites and M-sites on the basis of no any Mg–Al cation exchange (i.e., $x = 0$ for all P and T conditions); (b) Effects of Mg–Al cation exchange on the T-sites and M-sites. In (a), the relative variations of the T-sites and M-sites at some T and P conditions (represented by the filled squares), compared to those at zero K and 1 atm, are denoted by the numbers along the symbols, with the numbers in red for the T-sites and the numbers in black for the M-sites. The P-T conditions for the zero T-sites variation and zero M-sites variation are shown as the red line and black line, respectively. In addition, the P-T conditions of our high-P experiment are represented by the empty circles. According to Ma and Liu (2019), the effect of T on the T-sites and M-sites (i.e., thermal expansion) has been estimated from the neutron diffraction results obtained in the T-decreasing experiments below 900 K in Redfern et al. (1999), in which no any significant Mg–Al cation exchange reaction should have been triggered (i.e., u should be constant), and linearly extrapolated to higher T. Furthermore, the effect of P has been calculated from the equation of state determined by Nestola et al. (2007), which did not show any Mg–Al cation exchange reaction at room T (i.e., u was constant). For simultaneous high-P and high-T conditions, higher order effects of P and T have been ignored. In (b), the solid curves for the correlations between $d_{T\text{-}O}$ and x, and between $d_{M\text{-}O}$ and x are from Andreozzi et al. (2000; room P and T), and the broken extensions are extrapolations to both lower x and higher x. They were obtained from quenched samples, so that no thermal expansion effects were embedded. The equations used in the calculations were $d_{T\text{-}O} = a \times \sqrt[2]{3}(u - 0.125)$ and $d_{M\text{-}O} = a \times (3u^2 - 2u + 0.375)^{0.5}$ (Hill et al., 1979).

than those shown for the combined effects of P and T in Fig. 13a, implying a fundamentally important role for the cation exchange reaction in partitioning the trace elements.

Cation order-disorder phenomenon, triggered by P, T or composition variation, is well known for other geologically important minerals such as olivine, garnet, pyroxene and plagioclase (e.g., Carpenter et al., 1985; Cohen and Burnham, 1985; Redfern et al., 1996; Kelsey et al., 2008). How it affects the trace element partitioning behavior is largely unknown at the present, and requires extensive experimental investigation.

5. Conclusions

Our major conclusion from this study is that, for the spinel, the much large degrees of cation disordering induced by high P at high T can fundamentally alter the partitioning behavior of some trace elements such as Nb, Ta, Ti and the REEs. It thus suggests the effects of the cation disordering processes in other geologically important minerals on the trace element partitioning behaviors to be similarly experimentally explored.

Other conclusions include:

(1) The coupled substitution of $Si^{4+} + Mg^{2+} = 2Al^{3+}$ is important for the incorporation of Si in the spinel structure. Overall, Si is incompatible, with the D^{Si}_{Sp} values strongly dependent on the C^{Si}_{Sp} values ($D^{Si}_{Sp} = 8.71(23) \times 10^{-6} C^{Si}_{Sp}$ - 0.0028(4));
(2) Na is only mildly incompatible in the spinel. K, Ca, Sr and Ba are more strongly incompatible, presumably due to the larger cation radii. Rb is presumably incompatible as well, provided that the host spinel does not contain significant Mg vacancies;
(3) Cr and Ni are possibly much less compatible in the spinel at respectively Cr-poor and Ni-poor conditions than at respectively Cr-rich and Ni-rich conditions;
(4) Nb, Ta, and Ti are much more compatible in the spinels at high P than at low P, with the partition coefficients increased by orders of magnitudes; additionally, different coupled substitution reactions such as Nb^{4+} (Ta^{4+}, or Ti^{4+}) + Mg^{2+} = $2Al^{3+}$ and Nb^{4+} (Ta^{4+}, or Ti^{4+}) + V_{Mg} = $2Mg^{2+}$ may operate at different compositional conditions;
(5) U and Th are incompatible in the spinel but Pb appears compatible; in the CO_2-rich silicate magmas, most Pb cations probably occur in 4+, rather than in 2+;
(6) The REEs are much more compatible in the spinels at high P than at 1 atm, with the partition coefficients increased by several orders of magnitudes in general. Moreover, the partition coefficients of some heavy REEs may become larger than 1, leading to possible heavy REEs depletion in the coexisting magmas. These nominal P effects largely origin from the much larger degrees of cation disordering at high P, compared to those at 1 atm.

Acknowledgements

We thank two anonymous reviewers for their insightful comments which significantly improved this paper. This study was financially supported by the DREAM project of MOST, China (Grant No. 2016YFC0600408), by the Strategic Priority Research Program (B) of Chinese Academy of Sciences (Grant

No. XDB18000000), and by the Program of the Data Integration and Standardization in the Geological Science and Technology from MOST, China (Grant No. 2013FY1109000-3).

References

Andreozzi, G.B., Princivalle, F., Skogby, H., Della Giusta, A., 2000. Cation ordering and structural variations with temperature in $MgAl_2O_4$ spinel: an X-ray single-crystal study. Am. Mineral. 85, 1164–1171.

Arai, S., 1992. Chemistry of chromian spinel in volcanic-rocks as a potential guide to magma chemistry. Mineral. Mag. 56, 173–184.

Ballhaus, C., Berry, R.F., Green, D.H., 1991. High pressure experimental calibration of the olivine-orthopyroxene-spinel oxygen barometer: implications for the oxidation state of the upper mantle. Contrib. Mineral. Petrol. 107, 27–40.

Barnes, S.J., 1998. Chromite in komatiites, 1. Magmatic controls on crystallization and composition. J. Petrol. 39, 1689–1720.

Barnes, S.J., Roeder, P.L., 2001. The range of spinel compositions in terrestrial mafic and ultramafic rocks. J. Petrol. 42, 2279–2302.

Beattie, P., 1993. On the occurrence of apparent non-Henry's law behaviour in experimental partitioning studies. Geochem. Cosmochim. Acta 57, 47–55.

Bindeman, I.N., Davis, A.M., 2000. Trace element partitioning between plagioclase and melt: investigation of dopant influence on partition behavior. Geochem. Cosmochim. Acta 64, 2863–2878.

Blundy, J.D., Wood, B.J., 1994. Prediction of crystal-melt partition coefficients from elastic moduli. Nature 372, 452–454.

Brenan, J.M., Finnigan, C.F., McDonough, W.F., Homolova, V., 2012. Experimental constraints on the partitioning of Ru, Rh, Ir, Pt and Pd between chromite and silicate melt: the importance of ferric iron. Chem. Geol. 302, 16–32.

Brice, J.C., 1975. Some thermodynamic aspects of the growth of strained crystals. J. Cryst. Growth 28, 249–253.

Burnham, A.D., Berry, A.J., Wood, B.J., Cibin, G., 2012. The oxidation states of niobium and tantalum in mantle melts. Chem. Geol. 330–331, 228–232.

Canil, D., Scarfe, C.M., 1990. Phase relations in peridotite + CO_2 system to 12 GPa: implications to the origin of kimberlite and carbonate stability in the Earth's upper mantle. J. Geophys. Res. 95, 15805–15816.

Capobianco, C.J., Drake, M.J., 1990. Partitioning of ruthenium, rhodium, and palladium between spinel and silicate melt and implications for platinum group element fractionation trends. Geochem. Cosmochim. Acta 54, 869–874.

Capobianco, C.J., Hervig, R.L., Drake, M.J., 1994. Experiments on crystal liquid partitioning of Ru, Rh and Pd for magnetite and hematite solid-solutions crystallized from silicate melt. Chem. Geol. 113, 23–43.

Carpenter, M.A., McConnell, J.D.C., Navrotsky, A., 1985. Enthalpies of Al/Si ordering in the plagioclase feldspar solid solution. Geochem. Cosmochim. Acta 49, 947–966.

Cartier, C., Hammouda, T., Boyet, M., Mathon, O., Testemale, D., Moine, B.N., 2015. Evidence for Nb^{2+} and Ta^{3+} in silicate melts under highly reducing conditions: a XANES study. Am. Mineral. 100, 2152–2158.

Cohen, R.E., Burnham, C.W., 1985. Energetics of ordering in aluminous pyroxenes. Am. Mineral. 70, 559–567.

Cookenboo, H., Bustin, R., Wilks, K., 1997. Detrital chromian spinel compositions used to reconstruct the tectonic setting of provenance: implications for orogeny in the Canadian Cordillera. J. Sediment. Res. 67, 116–123.

Cynn, H., Anderson, O.L., Nicol, M., 1993. Effects of cation disordering in a natural $MgAl_2O_4$ spinel observed by rectangular parallelepiped ultrasonic resonance and Raman measurements. Pure Appl. Geophys. 141, 415–444.

Cynn, H., Sharma, S.K., Cooney, T.F., Nicol, M., 1992. High-temperature Raman investigation of order-disorder behavior in the $MgAl_2O_4$ spinel. Phys. Rev. B 45, 500–502.

Dalton, J.A., Presnall, D.C., 1998. The continuum of primary carbonatitic–kimberlitic melt compositions in equilibrium with lherzolite: data from the system CaO-MgO-Al_2O_3-SiO_2-CO_2 at 6 GPa. J. Petrol. 39, 1953–1964.

Da Rocha, S., Thibaudeau, P., 2003. Ab initio high-pressure thermodynamics of cationic disordered $MgAl_2O_4$ spinel. J. Phys. Condens. Matter 15, 7103–7115.

Davis, F.A., Humayun, M., Hirschmann, M.M., Cooper, R.S., 2013. Experimentally determined mineral/melt partitioning of first-row transition elements (FRTE) during partial melting of peridotite at 3 GPa. Geochem. Cosmochim. Acta 104, 232–260.

De Wijs, G.A., Fang, C.M., Kresse, G., de With, G., 2002. First-principles calculation of the phonon spectrum of $MgAl_2O_4$ spinel. Phys. Rev. B 65, 094305.

Dick, H.J.B., Bullen, T., 1984. Chromian spinel as a petrogenetic indicator in abyssal and alpine-type peridotites and spatially associated lavas. Contrib. Mineral. Petrol. 86, 54–76.

Draper, D.S., Xirouchakis, D., Agee, C.B., 2003. Trace element partitioning between garnet and chondritic melt from 5 to 9 GPa: implications for the onset of the majorite transition in the martian mantle. Phys. Earth Planet. In. 139, 149–169.

Fabriès, J., 1979. Spinel-olivine geothermometry in peridotites from ultramafic complexes. Contrib. Mineral. Petrol. 69, 329–336.

Graham, J., 1978. Manganochromite, palladium antimonide, and some unusual mineral associations at the Nairne pyrite deposit, South Australia. Am. Mineral. 63, 1166–1174.

Gross, J., Treiman, A.H., 2011. Unique spinel-rich lithology in lunar meteorite ALHA81005: origin and possible connection to M3 observations of the farside highlands. J. Geophys. Res. 116, E10009.

Gudfinnsson, G.H., Presnall, D.C., 1996. Melting relations of model lherzolite in the system CaO-MgO-Al_2O_3-SiO_2 at 2.4-3.4 GPa and the generation of komatiites. J. Geophys. Res. 101, 27701–27709.

Harrison, W.L., Wood, B.J., 1980. An experimental investigation of the partitioning of REE between garnet and liquid with reference to the role of defect equilibria. Contrib. Mineral. Petrol. 72, 145–155.

Hazen, R.M., Finger, L.W., 1979. Bulk modulus-volume relationships for cation-anion polyhedra. J. Geophys. Res. 84, 6723–6728.

He, Q., Liu, X., Hu, X., Li, S., Wang, H., 2011. Solid solution between lead fluorapatite and lead fluorvanadate apatite: mixing behavior, Raman feature and thermal expansivity. Phys. Chem. Miner. 38, 741–752.

He, Q., Tang, J.J., Wang, F., Liu, X., 2014. High temperature stable assembly designed for cubic press. Chin. J. High Press. Phys. 28, 145–151.

Herrmann, W., Berry, R.F., 2002. MINSQ - a least squares spreadsheet method for calculating mineral proportions from whole rock major element analyses. Geochem. Explor. Environ. Anal. 2, 361–368.

Hill, R.J., Craig, J.R., Gibbs, G.V., 1979. Systematics of the spinel structure type. Phys. Chem. Miner. 4, 317–339.

Horn, I., Foley, S.F., Jackson, S.E., Jenner, G.A., 1994. Experimentally determined partitioning of high-field strength-elements and selected transition-elements between spinel and basaltic melts. Chem. Geol. 117, 193–218.

Hu, X., Bi, X., Hu, R., Cai, G., Chen, Y., 2016. Tin partition behavior and implications for the Furong tin ore formation associated with peralkaline intrusive granite in Hunan Province, China. Acta. Geochim. 35, 138–147.

Imai, T., Takahashi, E., Suzuki, T., Hirata, T., 2012. Element partitioning between olivine and melt up to 10 GPa: implication for the effect of pressure. Phys. Earth Planet. In. 212–213, 64–75.

Jackson, S.E., 2001. The application of Nd: YAG lasers in LA-ICP-MS. Principles and applications of laser ablation-mass spectrometry in the earth. In: Mineralogical Association of Canada Short Course Series, vol. 29, pp. 29–46.

Jiang, S., Liu, J., Bai, L., Li, X., Li, Y., He, S., Yan, S., Liang, D., 2018. Anomalous compression behaviour in Nd_2O_3 studied by x-ray diffraction and Raman spectroscopy. AIP Adv. 8, 025019.

Jochum, K.P., Weis, U., Stoll, B., Kuzmin, D., Yang, Q., Raczek, I., Jacob, D.E., Stracke, A., Birbaum, K., Frick, D.A., Gunther, D., Enzweiler, J., 2011. Determination of reference values for NIST SRM 610-617 glasses following ISO guidelines. Geostand. Geoanal. Res. 35, 397–429.

Jones, J.H., 2016. Thoughts and reminiscences on experimental trace element partitioning. Geochem. Perspect. 5, 147−251.
Kamenetsky, V.S., Crawford, A.J., Meffre, S., 2001. Factors controlling chemistry of magmatic spinel: an empirical study of associated olivine, Cr-spinel and melt inclusions from primitive rocks. J. Petrol. 42, 655−671.
Kelsey, K.E., Stebbins, J.F., Du, L.-S., Mosenfelder, J.L., Asimow, P.D., Geiger, C.A., 2008. Cation order/disorder behavior and crystal chemistry of pyrope-grossular garnets: an ^{17}O 3QMAS and ^{27}Al MAS NMR spectroscopic study. Am. Mineral. 93, 134−143.
Law, K.M., Blundy, J.D., Wood, B.J., Ragnarsdottir, K.V., 2000. Trace element partitioning between wollastonite and carbonate-silicate melt. Mineral. Mag. 64, 651−661.
Lazartigues, A.V., Sirois, P., Savard, D., 2014. LA-ICP-MS analysis of small samples: carbonate reference materials and larval fish otoliths. Geostand. Geoanal. Res. 38, 225−240.
Lazzeri, M., Thibaudeau, P., 2006. Ab initio Raman spectrum of the normal and disordered $MgAl_2O_4$ spinel. Phys. Rev. B 74, 2952−2961.
Li, J., Kornprobst, J., Vielzeuf, D., Fabriès, J., 1995. An improved experimental calibration of the olivine-spinel geothermometer. Chin. J. Geochem. 14, 68−77.
Liu, J., Dauphas, N., Roskosz, M., Hu, M.Y., Yang, H., Bi, W., Zhao, J., Alp, E.E., Hu, J.Y., Lin, J.-F., 2016. Iron isotopic fractionation between silicate mantle and metallic core at high pressure. Nat. Commun. 8, 14377.
Liu, L.P., Liu, X., Bao, X.J., He, Q., Yan, W., Ma, Y.L., He, M.Y., Tao, R.B., Zou, R.Q., 2018. Si-disordering in $MgAl_2O_4$-spinel under high P-T conditions, with implications for Si-Mg disorder in Mg_2SiO_4-ringwoodite. Minerals 8, 210.
Liu, T.C., Presnall, D.C., 1990. Liquidus phase relationships on the join anorthite-forsterite-quartz at 20 kbar with applications to basalt petrogenesis and igneous sapphirine. Contrib. Mineral. Petrol. 104, 735−742.
Liu, X., Chen, J., Tang, J., He, Q., Li, S., Peng, F., He, D., Zhang, L., Fei, Y., 2012. A large volume cubic press with a pressure-generating capability up to about 10 GPa. High Press. Res. 32, 239−254.
Liu, X., O'Neill, H.St.C., 2004a. The effect of Cr_2O_3 on the partial melting of spinel lherzolite in the system CaO-MgO-Al_2O_3-SiO_2-Cr_2O_3 at 1.1 GPa. J. Petrol. 45, 2261−2286.
Liu, X., O'Neill, H.St.C., 2004b. Partial melting of spinel lherzolite in the system CaO-MgO-Al_2O_3-SiO_2 ± K_2O at 1.1 GPa. J. Petrol. 45, 1339−1368.
Liu, X., O'Neill, H.St.C., Berry, A.J., 2006. The effects of small amounts of H_2O, CO_2 and Na_2O on the partial melting of spinel lherzolite in the system CaO-MgO-Al_2O_3-SiO_2 ± H_2O ± CO_2 ± Na_2O at 1.1 GPa. J. Petrol. 47, 409−434.
Liu, X., Shieh, S.R., Fleet, M.E., Akhmetov, A., 2008. High-pressure study on lead fluorapatite. Am. Mineral. 93, 1581−1584.
Liu, X., Xiong, Z., Shieh, S.R., He, Q., Deng, L., Zhang, Y., Chang, L., Wang, F., Hong, X., Chen, Z., 2016. Non-monotonic compositional dependence of isothermal bulk modulus of the $(Mg_{1-x}Mn_x)Cr_2O_4$ spinel solid solutions, and its origin and implication. Solid Earth Sci. 1, 89−100.
Li, X., Mo, X., Yu, X., Ding, Y., Huang, X., Wei, P., He, W., 2013. Petrology and geochemistry of the early mesozoic pyroxene andesites in the Maixiu Area, west Qinling, China: products of subduction or syn-collision? Lithos 172−173, 158−174.
Loroch, D., Klemme, S., Berndt, J., Rohrbach, A., 2018. Experimentally determined trace element partition coefficients between hibonite, melilite, spinel, and silicate melts. Data Brief 21, 2447−2463.
Lundstrom, C.C., Sutton, A.L., Chaussidon, M., McDonough, W.F., Ash, R.D., 2006. Trace element partitioning between type B CAI melts and melilite and spinel: implications for trace element distribution during CAI formation. Geochem. Cosmochim. Acta 70, 3421−3435.
Mallmann, G., O'Neill, H.St.C., 2009. The crystal/melt partitioning of V during mantle melting as a function of oxygen fugacity compared with some other elements (Al, P, Ca, Sc, Ti, Cr, Fe, Ga, Y, Zr and Nb). J. Petrol. 50, 1765−1794.
Ma, Y., Liu, X., 2019. Kinetics and thermodynamics of Mg-Al disorder in $MgAl_2O_4$-Spinel: a Review. Molecules 24, 1704.
Méducin, F., Redfern, S.A.T., Godec, Y.L., Stone, H.J., Tucker, M.G., Dove, M.T., Marshall, W.G., 2004. Study of cation order-disorder in $MgAl_2O_4$ spinel by in situ neutron diffraction up to 1600 K and 3.2 GPa. Am. Mineral. 89, 981−986.
Mi, Z., Shi, W., Zhang, L., Shieh, S.R., Liu, X., 2018. Equation of state of a natural chromian spinel at ambient temperature. Minerals 8, 591.
Nagasawa, H., Schreiber, H.D., Morris, R.V., 1980. Experimental mineral/liquid partition coefficients of the rare Earth elements, Sc and Sr for perovskite, spinel and melilite. Earth Planet. Sci. Lett. 46, 431−437.
Nernst, W., 1891. Distribution of a substance between two solvents and between solvent and vapor. Z. Phys. Chem. 163, 142−154.
Nestola, F., Ballaran, T.B., Zunic, T.B., Princivalle, F., Secco, L., Negro, A.D., 2007. Comparative compressibility and structural behavior of spinel $MgAl_2O_4$ at high pressures: the independency on the degree of cation order. Am. Mineral. 92, 1838−1843.
Nielsen, R.L., Beard, J.S., 2000. Magnetite-melt HFSE partitioning. Chem. Geol. 164, 21−34.
Nielsen, R.L., Forsythe, L.M., Gallahan, W.E., Fisk, M.R., 1994. Major- element and trace element magnetite-melt equilibria. Chem. Geol. 117, 167−191.
Nielsen, R.L., Gallahan, W.E., Newberger, F., 1992. Experimentally determined mineral-melt partition-coefficients for Sc, Y and REE for olivine, orthopyroxene, pigeonite, magnetite and ilmenite. Contrib. Mineral. Petrol. 110, 488−499.
O'Neill, H.St.C., 1981. The transition between spinel lherzolite and garnet lherzolite, and its use as a geobarometer. Contrib. Mineral. Petrol. 77, 185−194.
O'Neill, H.St.C., Wall, V.J., 1987. The olivine-orthopyroxene-spinel oxygen geo-barometer, the nickel precipitation curve, and the oxygen fugacity of the Earth's upper mantle. J. Petrol. 28, 1169−1191.
Paraskevopoulos, G.M., Economou, M., 1981. Zoned Mn-rich chromite from podiform type chromite ore in serpentinites of northern Greece. Am. Mineral. 66, 1013−1019.
Pieters, C.M., Besse, S., Boardman, J., Buratti, B., Cheek, L., Clark, R.N., Combe, J.P., Dhingra, D., Goswami, J.N., Green, R.O., Head, J.W., Isaacson, P., Klima, R., Kramer, G., Lundeen, S., Malaret, E., McCord, T., Mustard, J., Nettles, J., Petro, N., Runyon, C., Staid, M., Sunshine, J., Taylor, L.A., Thaisen, K., Tompkins, S., Whitten, J., 2011. Mg-spinel lithology: a new rock type on the lunar farside. J. Geophys. Res. 116, 287−296.
Polyakov, V.B., 2009. Equilibrium iron isotope fractionation at core-mantle boundary conditions. Science 323, 912−914.
Presnall, D.C., Dixon, S.A., Dixon, J.R., O'Donnell, T.H., Brenner, N.L., Schrock, R.L., Dycus, D.W., 1978. Liquidus phase relations on the joint diopside-forsterite-anorthite from 1 atm to 20 kbar: their bearing on the generation and crystallization of basaltic magma. Contrib. Mineral. Petrol. 66, 203−220.
Redfern, S.A.T., Harrison, R.J., O'Neill, H.St.C., Wood, D.R.R., 1999. Thermodynamics and kinetics of cation ordering in $MgAl_2O_4$ spinel up to 1600 °C from in situ neutron diffraction. Am. Mineral. 84, 299−310.
Redfern, S.A.T., Henderson, C.M.B., Wood, B.J., Harrison, R.J., Knight, K.S., 1996. Determination of olivine cooling rates from metal-cation ordering. Nature 381, 407−409.
Righter, K., Campbell, A.J., Humayun, M., Hervig, R.L., 2004. Partitioning of Ru, Rh, Pd, Re, Ir, and Au between Cr-bearing spinel, olivine, pyroxene and silicate melts. Geochem. Cosmochim. Acta 68, 867−880.
Righter, K., Leeman, W.P., Hervig, R.L., 2006. Partitioning of Ni, Co and V between spinel-structured oxides and silicate melts: importance of spinel composition. Chem. Geol. 227, 1−25.
Roeder, P.L., 1994. Chromite: from the fiery rain of chondrules to the Kilauea Iki lava lake. Can. Mineral. 32, 729−746.
Roeder, P.L., Reynolds, I., 1991. Crystallization of chromite and chromium solubility in basaltic melts. J. Petrol. 32, 909−934.
Salters, V.J., Longhi, J.E., Bizimis, M., 2002. Near mantle solidus trace element partitioning at pressures up to 3.4 GPa. Geochem. Geophys. Geosyst. 3.
Sen, G., Presnall, D.C., 1984. Liquidus phase relationships on the join anorthite-forsterite-quartz at 10 kbar with applications to basalt petrogenesis. Contrib. Mineral. Petrol. 85, 404−408.
Shannon, R.D., 1976. Revised effective ionic radii and systematic studies of interatomic distances in halides and chalcogenides. Acta Crystallogr. 32, 751−767.

Slotznick, S.P., Shim, S.H., 2008. In situ Raman spectroscopy measurements of $MgAl_2O_4$ spinel up to 1400 °C. Am. Mineral. 93, 470−476.

Taylor, P.D.P., Maeck, R., De Bièvre, P., 1992. Determination of the absolute isotopic composition and atomic weight of a reference sample of natural iron. Int. J. Mass Spectrom. 121, 111−125.

Van Minh, N., Yang, I.S., 2004. A Raman study of cation-disorder transition temperature of natural $MgAl_2O_4$ spinel. Vib. Spectrosc. 35, 93−96.

Wang, S., Liu, X., Fei, Y., He, Q., Wang, H., 2012. In situ high-temperature powder X-ray diffraction study on the spinel solid solutions $(Mg_{1-x}Mn_x)Cr_2O_4$. Phys. Chem. Miner. 39, 189−198.

Watson, E.B., 1985. Henry's law behavior in simple systems and in magmas: criteria for discerning concentration-dependent partition coefficients in nature. Geochem. Cosmochim. Acta 49, 917−923.

Wijbrans, C.H., Klemme, S., Berndt, J., Vollmer, C., 2015. Experimental determination of trace element partition coefficients between spinel and silicate melt: the influence of chemical composition and oxygen fugacity. Contrib. Mineral. Petrol. 169, 45−77.

Williams, H.M., McCammon, C.A., Peslier, A.H., Halliday, A.N., Teutsch, N., Levasseur, S., Burg, J.-P., 2004. Iron isotope fractionation and the oxygen fugacity of the mantle. Science 304, 1656−1659.

Wood, B.J., Blundy, J.D., 1997. A predictive model for rare earth element partitioning between clinopyroxene and anhydrous silicate melt. Contrib. Mineral. Petrol. 129, 166−181.

Zhang, Y., Liu, X., Xiong, Z., Zhang, Z., 2016. Compressional behavior of $MgCr_2O_4$ spinel from first-principles simulation. Sci. China Earth Sci. 59, 989−996.